Research Paper

Nuclear inclusions of pathogenic ataxin-1 induce oxidative stress and perturb the protein synthesis machinery

Stamatia Laidou[a], Gregorio Alanis-Lobato[b,c], Jan Pribyl[d], Tamás Raskó[e], Boris Tichy[d], Kamil Mikulasek[d,f], Maria Tsagiopoulou[a], Jan Oppelt[d], Georgia Kastrinaki[g], Maria Lefaki[h], Manvendra Singh[e], Annika Zink[e,i], Niki Chondrogianni[h], Fotis Psomopoulos[a,j], Alessandro Prigione[e,i], Zoltán Ivics[k], Sarka Pospisilova[d], Petr Skladal[d], Zsuzsanna Izsvák[e,**], Miguel A. Andrade-Navarro[b], Spyros Petrakis[a,*]

[a] Institute of Applied Biosciences/Centre for Research and Technology Hellas, 57001, Thessaloniki, Greece
[b] Faculty of Biology, Johannes Gutenberg University Mainz, 55122, Mainz, Germany
[c] Human Embryo and Stem Cell Laboratory, The Francis Crick Institute, NW1 1AT, London, UK
[d] Central European Institute of Technology, Masaryk University, 62500, Brno, Czech Republic
[e] Max-Delbrueck-Center for Molecular Medicine in the Helmholtz Association, Berlin, 13125, Germany
[f] National Centre for Biomolecular Research, Faculty of Science, Masaryk University, 62500, Brno, Czech Republic
[g] Aerosol and Particle Technology Laboratory/Chemical Process & Energy Resources Institute/Centre for Research and Technology Hellas, 57001, Thessaloniki, Greece
[h] Institute of Biology, Medicinal Chemistry & Biotechnology/National Hellenic Research Foundation, 11365, Athens, Greece
[i] Department of General Pediatrics, Neonatology and Pediatric Cardiology, University Children's Hospital, Heinrich Heine University, 40225, Düsseldorf, Germany
[j] Department of Molecular Medicine and Surgery, Karolinska Institutet, 17177, Stockholm, Sweden
[k] Division of Medical Biotechnology, Paul-Ehrlich-Institute, 63225, Langen, Germany

ARTICLE INFO

ABSTRACT

Spinocerebellar ataxia type-1 (SCA1) is caused by an abnormally expanded polyglutamine (polyQ) tract in ataxin-1. These expansions are responsible for protein misfolding and self-assembly into intranuclear inclusion bodies (IIBs) that are somehow linked to neuronal death. However, owing to lack of a suitable cellular model, the downstream consequences of IIB formation are yet to be resolved. Here, we describe a nuclear protein aggregation model of pathogenic human ataxin-1 and characterize IIB effects. Using an inducible *Sleeping Beauty* transposon system, we overexpressed the *ATXN1(Q82)* gene in human mesenchymal stem cells that are resistant to the early cytotoxic effects caused by the expression of the mutant protein. We characterized the structure and the protein composition of insoluble polyQ IIBs which gradually occupy the nuclei and are responsible for the generation of reactive oxygen species. In response to their formation, our transcriptome analysis reveals a cerebellum-specific perturbed protein interaction network, primarily affecting protein synthesis. We propose that insoluble polyQ IIBs cause oxidative and nucleolar stress and affect the assembly of the ribosome by capturing or down-regulating essential components. The inducible cell system can be utilized to decipher the cellular consequences of polyQ protein aggregation. Our strategy provides a broadly applicable methodology for studying polyQ diseases.

1. Introduction

Polyglutamine (polyQ) diseases are neurodegenerative disorders caused by trinucleotide (CAG) repeat expansions in the coding region of human genes, which result in abnormally large polyQ tracts in the produced proteins. In spinocerebellar ataxia type-1 (SCA1), the disease is caused by CAG expansions in the *ATXN1* gene [1]. The polyQ-expanded ataxin-1 (ATXN1) protein forms small oligomers and slowly

aggregates into larger insoluble nuclear inclusions in the affected neurons [2]. These are specifically detectable in the Purkinje cells of the cerebellum in SCA1 patients [1]. Several lines of evidence suggest that the deposition of large inclusions may be protective due to the sequestration of smaller cytotoxic oligomers [3]. However, recent findings indicate that insoluble inclusions might be also toxic, as they cause quiescence and activate necrotic mechanisms in cells [4]. These events are thought to be induced by oxidative stress and the activation of checkpoint kinases which regulate the cell cycle [5].

PolyQ aggregates have been extensively investigated in cell-free assays, using recombinant proteins produced in bacteria [6–8]. Studies in yeast, murine neurons and HeLa cells overexpressing fragments of polyQ-expanded genes provided valuable information on the structure and interactions of pathogenic inclusions in cellular systems [9,10]. However, a reliable aggregation model is still missing. While formation of insoluble inclusions was also observed in human induced pluripotent stem cell (iPSC)-derived neurons [11], this phenotype cannot be easily reproduced [12]. Therefore, novel protein aggregation models are needed that could be readily used to characterize polyQ inclusions generated in primary human cells.

Human mesenchymal stem cells (MSCs) have been previously used for modeling of polyQ diseases [13]. These cells have a partial ability to fuse with Purkinje neurons [14], suggesting that they might contribute to the restoration of their physiological neuronal function. MSCs can be easily modified genetically using the *Sleeping Beauty* (SB) transposon system [15], a safer alternative to viral approaches [16]. Engineered cells proliferate and stably express human transgenes for several passages [17–19]. MSCs can also model replicative senescence, a cellular event that resembles aging and is associated with protein aggregation [20]. Expression of aberrant, polyQ-expanded genes in human MSCs is expected to generate suitable cellular models supporting robust, measurable and reproducible pathogenic phenotypes.

In this study, we report an inducible version of a previously described SB system [21] that can be utilized for the controlled expression of pathogenic genes in cultured primary cells. We used this system to overexpress polyQ-expanded *ATXN1* in human MSCs and observed that cells reproducibly accumulate intranuclear inclusion bodies (IIBs). First, the IIBs generate cellular oxidative stress and following prolonged induction become insoluble. Using a combination of biophysical methods [Fourier-transform infrared spectroscopy (FTIR), atomic force microscopy (AFM) and mass spectrometry (MS)], we characterized their structure and protein composition. In addition, we analyzed transcriptional changes and mechanisms of dysfunction caused by the overexpression of mutant *ATXN1* and the gradual accumulation of its protein product. We assessed the similarity of this model with human SCA1 cerebellum at the end-stage of the disease in terms of mechanisms leading to disease. In particular, our data indicate that aggregation of pathogenic ATXN1 perturbs the cellular protein synthesis machinery in a cerebellar protein-protein interaction (PPI) network. The potential implications of these results for the homeostasis of cerebellar neurons are discussed.

2. Materials and methods

2.1. Construction of Tet-On Sleeping Beauty transposon plasmids

For the generation of a pT2-CMV/TetO$_2$-EYFP-GW transposon plasmid, the CMV promoter was excised by HindIII-NheI digestion from a pT2-CMV-EYFP-GW plasmid [21] and replaced by a CMV/TetO$_2$ promoter. *ATXN1(Q30)* (wild-type *ATXN1*; GeneID: 6310) or *(Q82)* cDNA was shuttled into pT2-CMV/TetO$_2$-EYFP-GW plasmid by LR recombination, as previously described [22]. Correct recombination was verified by BsrGI restriction digestion.

An expression cassette encoding the SV40 promoter, β-globin intron, Tet-repressor (TetR) and bGH polyA signal flanked by SpeI restriction sites was synthesized and cloned into a pU57C plasmid. The cassette was subcloned by SpeI digestion into the MCS of a pT2-HB plasmid resulting in the generation of a pT2-TetR plasmid. Then, an expression cassette encoding the SV40 promoter, neomycin resistance gene (neo^R) and SV40 polyA site was excised by HindIII from a pT2-neo^R plasmid and inserted into the pT2-TetR plasmid, resulting in the generation of a bicistronic pT2-TetR-neo^R transposon. The orientation of TetR and neo^R expression cassettes was verified by EcoRV digestion. Plasmid isolation was performed using a DNA plasmid purification kit (Macherey-Nagel).

2.2. MSC and neural precursor cell (NPC) culture

Isolation and characterization of human MSCs have been previously described [17,18]. Cells were cultured and expanded *ex-vivo* using Dulbecco's modified Eagle medium (DMEM) supplemented with 10% fetal bovine serum, penicillin (100 IU/mL) and streptomycin (100 μg/mL). NPCs were obtained from healthy human iPSCs as previously described [23]. Cells were seeded on Matrigel-coated plates and cultured in DMEM-F12/NeuroCult 1:1 supplemented with 1:200 N2 supplement, 1:100 B27 supplement lacking vitamin A, 3 μM CHIR 99021, 0.5 μM purmorphamine, 150 μM ascorbic acid (Sigma-Aldrich) and 1% penicillin/streptomycin/glutamine [24].

2.3. Generation of stable cell lines

MSCs at passage 5 or NPCs at passage 9 were transfected with a mixture of SB100X/pT2 plasmids using Xfect reagent (Clontech), according to manufacturer's instructions. Briefly, 2×10^5 cells were seeded in a 6-well tissue culture plate. The next day, cells were transfected with 5 μg of total plasmid DNA encoding SB100X transposase and pT2 plasmids (1:9 ratio). The ratio of pT2-TetO$_2$-YFP-*ATXN1(Q30)* or *(Q82)* and pT2-TetR-neo^R transposon plasmids was 5:1. For the generation of MSCs stably producing Venus, a pT2-GAGGS-Venus-neo^R transposon plasmid was used. Transfected cells were selected at day 7 post-transfection with 100 μg/mL G418 and expanded in the presence of the antibiotic. For transgene induction, fresh doxycycline (Dox) (2 μg/mL) was added every 48hrs in the culture medium.

2.4. Immunofluorescence

Tet-On YFP-ATXN1(Q82) MSCs or NPCs were cultured in the presence or absence of doxycycline in CELLview glass bottom plates (Greiner Bio One). Then, cells were fixed with 4% paraformaldehyde (PFA) in PBS and permeabilized with 0.1% Triton-X 100 PBS before mounting with DAPI ProLong Gold antifade reagent (ThermoFisher). Cells were visualized in an Axiovert microscope equipped with an HBO 50 mercury lamp and reflectors with fluorescence filter sets. Image acquisition was performed with the Fluorescence Lite software module of AxioVision LE (Carl Zeiss).

2.5. Flow cytometry

For quantification of transgene expression, Tet-On YFP-ATXN1(Q82) MSCs were measured in a Cytomics FC500 flow cytometer (Beckman Coulter) using the CXP2.2 software. For phenotypic characterization, 1×10^6 cells were stained with antibodies against hemopoietic (CD34, 45) or mesenchymal (CD29, 73, 90 and CD105) stem cell markers. Unstained cells or cells stained with IgG isotype antibodies were used as negative controls.

2.6. Immunoblotting

MSCs (5×10^5) were lysed in 1% SDS PBS containing protease inhibitors (Calbiochem) and benzonase (Novagen). Cell extracts were analyzed in an 8% SDS-PAGE. Ectopic expression of YFP-*ATXN1(Q30)* or *(Q82)* was validated by Western blotting with the polyclonal anti-

ATXN1 SA4645 antibody [22] or anti-GFP antibody (MAB2510, Millipore). β-actin was detected with mouse monoclonal anti-β-actin antibody (sc-47778, Santa Cruz). After incubation with an appropriate alkaline-phosphatase conjugated secondary antibody, proteins were detected with NBT-BCIP (Applichem).

2.7. Filter retardation assay

Insoluble protein inclusions were quantified using a filter retardation assay [25]. Cell extracts of Tet-On YFP-ATXN1(Q30) or (Q82) MSCs (150 μg total protein) were mixed with equal volumes of 4% SDS and 100 mM DTT and heated at 95 °C for 5 min. Samples were diluted with 100 μl 0.2% SDS and filtered through a 0.2 μm cellulose acetate membrane. SDS-resistant inclusions retained on the membrane were detected using the polyclonal anti-ATXN1 SA4645 antibody (1:1000) [22].

2.8. FTIR spectroscopy

Tet-On YFP-ATXN1(Q82) MSCs were cultured on MirrIR low-e-glass slides (Kevley Technologies, USA) washed with PBS and air dried. The spectra were taken using a Renishaw-Smiths micro Raman-FTIR microscope (Smiths-IlluminatIR, Smiths Detection, Hertfordshire, UK) and an ARO microscope lens (smithsARO 15x/N.A.88) at a range of 600–4000 cm^{-1} wavenumbers with 100 measurements for the background spectrum and 300 for the sample spectrum with a 4 cm^{-1} resolution. The low-e glass slide was placed on an automated holder and exposed to the instrument hood-controlled temperature and humidity environment of 22 °C and 37%, respectively. Background and sample absorption spectra were taken at a 100 μm diameter circular region. The sample absorption spectrum was calculated after background subtraction using the SynchronizIR software (Soft Imaging System GmbH, Germany). The second derivative spectra were obtained by a 5-point Savitzky-Golay algorithm of the smoothed spectrum (11-point binomial) using the GRAMS/32 software (Galactic Industries Corporation, Salem, NH, USA), according to relative processing [26].

2.9. Cytotoxicity assay

Tet-On YFP-ATXN1(Q82) MSCs were cultured in 96-well tissue culture plates (2×10^4 per well). Equal volume of Caspase 3/7 Glo substrate (Promega) was added in each well and luminescence was measured in a Victor3 multilabel plate reader (PerkinElmer). Each experiment was performed in triplicate.

2.10. Detection of reactive oxygen species (ROS)

2′7′-Dichlorodihydrofluorescein diacetate (H2DCFDA) (ThermoFischer) was used for detection of ROS. Tet-On YFP-ATXN1(Q82) were resuspended in PBS with or without the dye at a final concentration of 10 μM (loading buffer) and incubated at 37 °C for 30 min. The loading buffer was removed, cells were resuspended in prewarmed complete medium and further incubated at 37 °C for 5 min. The absorption and emission of the oxidation product were measured at 493 and 520 nm, respectively. Each experiment was performed in triplicate.

2.11. Proteasome peptidase assay

Chymotrypsin-like (CT-L) proteasome activity was assayed in protein extracts with the hydrolysis of a specific fluorogenic peptide, namely LLVY-AMC, at 37 °C for 30 min, as previously described [27]. Proteasome activity was determined as the difference between the total activity in protein extracts and the remaining activity in the presence of 20 μM MG132. Fluorescence was measured using a VersaFluor fluorescence spectrophotometer (Bio-Rad). Protein concentrations were determined using the Bradford method with bovine serum albumin as standard.

2.12. Preparation of samples for AFM

Cells were either kept in culture medium or fixed with 4% PFA PBS before observation. For imaging of nuclei, Tet-On YFP-ATXN1(Q82) MSCs were treated as previously described [28]. In brief, AFM images of nuclei were obtained by cell lysis in 0.25% NP-40 hypotonic Tris-HCl pH 7.4 buffer followed by fixation. For observation of polyQ inclusions, cells were lysed in 0.1% SDS PBS and purified inclusions attached to the plastic surface were immersed in PBS.

2.13. AFM imaging and mechanical characterization of nuclear content

Hybrid mode imaging, contact mode and Young's modulus mapping were performed using either Bruker Dimension FastScan (Bruker Nano Surfaces) AFM or JPK NanoWizard 3 (JPK). Bruker SCANASYST-FLUID + and SNL-10 A and B silicon nitride cantilevers equipped with silicon tip (both from Bruker Nano Surfaces) were used for imaging. Sensitivity and cantilever spring constant were calibrated by the routine procedure recommended by the instrument producer.

Hybrid mode imaging (Bruker QNM mode) with SCANASYST-FLUID + probe was employed to record semi-quantitative images of isolated nucleus in PBS buffer. Images covering an area of 15 × 15 μm^2 and 2.5 × 2.5 μm^2 area (1500 × 1500 px^2 resolution) were recorded with a set point of 0.75 nN and lifting height of 150 nm, (Z-piezo range 0.75 μm and 0.35 μm, respectively). Images covering the whole nucleus (20 × 20 μm^2, 1024 × 1024 px^2 resolution) as well as the detailed view of 5 × 5 and 2 × 2 μm^2 were recorded by JPK Quantitative Imaging mode (hybrid mode) with a set point of 0.35 nN and lifting height of 90 nm (Z-piezo range was shortened to 3.0 μm).

Cells fixed on a standard microscopic glass slide were visualized by constant force contact mode (JPK NanoWizard 3), when the Bruker SNL-10A cantilever was used. Set-point equal to 5.0 nN, feedback setting iGain = 50.0 Hz and PGain = 0.001 were the operating parameters for capturing images of 50 × 50, 25 × 25 and 10 × 10 μm^2 (2048 × 2048 px^2).

For mapping of Young's modulus of living cells a previously published procedure [29,30] was adopted. Briefly, Bruker SNL-10B probe was used to record 64 × 64 maps of force-distance curves (set-point 1 nN, Z-length 15 μm, time per curve 0.5 s). The recorded force-distance (FD) curves were fitted with the Bilodeau modification of the Hertzian model. Final post-processing and editing of the images and stiffness maps was performed using the Gwyddion software ver. 2.44 [31].

2.14. Force-distance curves post-processing

Force mapping provides a network of force-distance curves, measuring the dependence of the tip-sample interaction force on the tip height above the surface. The absolute value of Young's modulus can be determined by fitting the FD curve to the modified Hertzian-Sneddon equation:

$$F(\delta) = \frac{2E\tan\alpha}{\pi\,(1-\upsilon^2)}\delta$$

where F is the measured force, E is the Young's modulus, υ is the Poisson's ratio (0.5 for incompressible materials), δ is the tip-sample separation (obtained by correction of the cantilever height to its bending) and α is the half-angle to face of pyramidal tip (reflects the tip geometry). The data processing module of the JPK software was used to process the maps of FD curves. The resulting Young's modulus maps were exported in order to be post-processed using the Gwyddion software. Data masking and final export of stiffness maps were performed also using the Gwyddion software.

2.15. Mass spectrometry

For proteomic analysis of insoluble polyQ inclusions, Tet-On YFP-ATXN1(Q82) MSCs at D10 were lysed in 0.1% SDS PBS. Intact fluorescent polyQ inclusions were sorted from cell extracts in a BD FACSAria IIu instrument (BD Biosciences) after doublet exclusion and using an unstained control sample to exclude possible autofluorescence. Protein samples were processed by the filter-aided sample preparation (FASP) method [32]. Proteins were alkylated, digested by trypsin on filter unit membrane and resulting peptides were eluted by ammonium bicarbonate buffer. The peptide mixture was dried under vacuum and transferred using peptide extraction procedure to TPX vial. LC-MS/MS analysis was done using the RSLCnano system (Thermo Fisher Scientific) on-line connected to Impact II Ultra-High Resolution Qq-Time-Of-Flight mass spectrometer (Bruker). The analytical column outlet was directly linked to the CaptiveSpray nanoBooster ion source (Bruker). MS and MS/MS spectra were acquired in a data-dependent strategy with 3 s long cycle time.

For quantitative mass spectrometry, technical triplicates of Tet-On YFP-ATXN1(Q82) MSCs at D10 or D0 were lysed in SDT buffer. LC-MS/MS analysis of peptide mixture was done using RSLCnano system (Thermo Fisher Scientific) on-line connected to Orbitrap Q-Exactive HF X system (Thermo Fisher Scientific). The analytical column outlet was directly linked to the Digital PicoView 550 (New Objective) ion source. ABIRD (Active Background Ion Reduction Device, ESI Source Solutions) was installed. MS data were acquired in a data-dependent strategy selecting up to top 20 precursors.

The analysis of the mass spectrometric data was carried out using Maxquant (version 1.6.3.3) with Andromeda search engine utilization. Search was done against the UniprotKB Human (version 20180912) and Maxquant's contamination databases (downloaded with given version). Mass tolerances for peptides and MS/MS fragments were 4.5–10 ppm and 0.05 Da, respectively. Oxidation of methionine, deamidation (N, Q) and protein N-terminal acetylation as optional modifications, carbamidomethylation (C) as fixed modification and two enzyme miss cleavages were set for search. Peptides and proteins with false discovery rate (FDR; q-value) < 1% were considered. Maxquant label free quantification algorithm (MaxLFQ) was applied for global data normalization [33] (minimal ratio count 1). MQ protein group list was processed via KNIME Analytics Platform (v. 3.7.1). Results have been deposited in the PRIDE Archive (https://www.ebi.ac.uk/pride/archive) under accession number PXD012709.

2.16. RNA-sequencing

Total RNA was extracted from Tet-On YFP-ATXN1(Q82) MSCs using the AllPrep DNA/RNA/miRNA Universal Kit (QIAGEN), according to manufacturer's instructions. For library preparation, mRNA was enriched from 250 ng total RNA using the NEBNext® Poly(A) mRNA Magnetic Isolation Module (New England Biolabs), according to manufacturer's protocol. Sequencing libraries were prepared from mRNA using SENSE Total RNA-seq Library Prep Kit (Lexogen), according to manufacturer's protocol. Single-end 75 bp sequencing was performed in a NextSeq 500 instrument (Illumina). In average, more than 30 million reads per time-point were obtained.

Post-mortem human cerebellum from a 74-year-old female SCA1 patient and an age-/sex-matched healthy individual (Sample ID: A136/02 and A158/14, respectively) were obtained from the MRC London Neurodegenerative Diseases Brain Bank. Total RNA was extracted from frozen samples using the Direct-zol RNA Kit (Zymo Research). An aliquot of total RNA was loaded on Total RNA Pico Chip and measured for its integrity using Bionalyzer 2100 (Agilent Technologies). Sequencing libraries were prepared using KAPA RNA HyperPrep with Ryboerase kit, according to manufacturer's instructions (Roche). High throughput single-indexed, paired-end 75 bp sequencing was performed in a HiSeq 4000 instrument (Illumina). RNA-seq data have been deposited in the

ArrayExpress database at EMBL-EBI (www.ebi.ac.uk/arrayexpress) under accession numbers E-MTAB-7713 and E-MTAB-7714.

2.17. Data analysis and visualization of RNA-seq data

The quality control was performed based on the FastQC software (Babraham Institute, Cambridge, UK). Samples with a low number of raw reads (less than 10 million per sample) were excluded from downstream analysis. Reads were trimmed and filtered using Trim Galore! and consequently aligned against the UCSC hg19 reference genome using the HISAT2 protocol [34]. Overall alignment rate for all samples ranged between 89% and 93%. Transcriptome assembly was performed using StringTie and differential expression calculation was performed using Ballgown. Gene expression levels were normalized to Fragments Per Kilobase of transcript per Million (FPKM).

Subsequent data analysis was carried out in the R environment. T-test was applied to compare FPKM levels between the two different groups. Hierarchical clustering analysis was performed applying the R package "gplots" and FPKMs were normalized to z-score. The agglomerative hierarchical clustering was performed using the Euclidean distance metric and the complete agglomeration method. To compute the principal components (PCs), the prcomp function was applied. Gene set enrichment analysis (GSEA) was calculated using the clusterProfiler R package [35]. Gene Ontology (GO) and Pathway enrichment analyses were performed using the online tool Enrichr where KEGG and PANTHER pathways were examined [36]. Venny 2.1 (BioinfoGP, CNB–CSIC, http://bioinfogp.cnb.csic.es/tools/venny/index.html) was utilized to overlap the differentially expressed genes from different comparisons.

2.18. Construction of a PPI network

The PPI network in which the products of differentially expressed (DE) genes participate was constructed using release 2 of the Human Integrated Protein-Protein Interaction rEference (HIPPIE) [37]. Only cerebellum-specific interactions with HIPPIE confidence scores of at least 0.63 (median of all scores in the database) were considered, which resulted in a network of 516 proteins.

2.19. Statistical analysis

Statistical analysis was performed using the GraphPad Prism software (San Diego, USA). All cell-based assays were performed in triplicates and results are shown as mean ± SEM calculated by a T-test. For AFM measurement of cell stiffness, a one-way ANOVA with Bonferroni post-hoc test was used.

To determine if the size of the largest connected component (LCC) of the constructed PPI network (328 proteins) was greater than expected by chance, it was compared with a distribution of LCC sizes using a z-test. This distribution resulted from randomly sampling 516 proteins 1,000 times from the complete cerebellum-specific PPI network. A z-test was also employed to determine if the number of DE genes, common to cells and the SCA1 patient and also present in the PPI network, was significantly larger than expected by chance. Specifically, we randomly sampled 185 genes from the 3,923 SCA1-differentially-expressed pool 1,000 times and intersected the sample with the 328 members of the PPI LCC. Then, we checked whether 109 (the actual size of the intersection between the 185 SCA1-DE genes and the LCC) was significantly greater than the constructed random distribution. Differences in protein levels of the network were investigated by LIMMA test. P-values were adjusted with the Benjamini-Hochberg method.
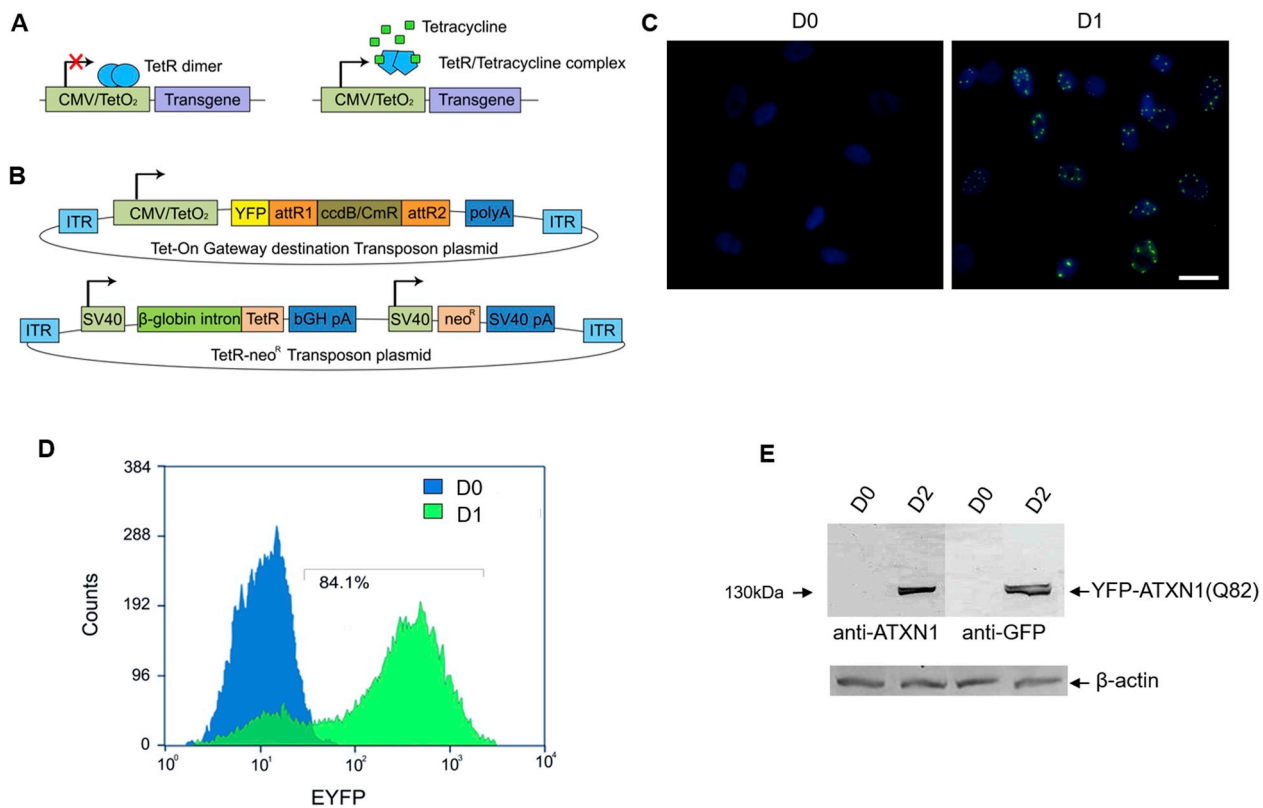
Fig. 1. Generation of Tet-On YFP-ATXN1(Q82) MSCs using a novel inducible SB transposon system. **(A)** Schematic overview of the Tet-On principle. In the absence of tetracycline, TetR protein dimers bind to the CMV/TetO$_2$ promoter and suppress transgene expression. In the presence of tetracycline, TetR adopts a different conformation and loses its affinity for the CMV/TetO$_2$ promoter allowing transgene expression. **(B)** Components of the Tet-On SB transposon system. The system is comprised of two pT2-based plasmids, a Tet-On Gateway compatible and a bicistronic TetR-neo[R] transposon. **(C)** Fluorescence microscopy of Tet-On YFP-ATXN1(Q82) MSCs in the absence (D0, left) or presence (D1, right) of Dox (scale bar = 25 μm). **(D)** Flow cytometry (histogram plot) of uninduced (blue color) and induced (green color) cells. **(E)** Immunoblot detection of transgene expression in extracts of uninduced and induced cells using anti-ATXN1 or anti-GFP antibodies. β-actin was used as a loading control. . (For interpretation of the references to color in this figure legend, the reader is referred to the Web version of this article.)

3. Results

3.1. Inducible Sleeping Beauty transposon system to express ATXN1 variants

In order to develop a stable *ATXN1* expression model, an inducible Tet-On SB transposon system was generated. The system consists of two pT2-based expression plasmids, a Tet-On YFP-tagged Gateway destination plasmid, in which *ATXN1(Q82)* was shuttled [resulting in YFP-*ATXN1(Q82)*], and a TetR-neo[R] bicistronic transposon plasmid encoding for the TetR protein and the neomycin resistance gene (Fig. 1A–B). Using the hyperactive SB100X transposase [15], a stable expression cell line was generated in human MSCs.

Tet-On YFP-ATXN1(Q82) MSCs displayed no fluorescent signal in the absence of the inducer Dox (D0), whereas inducing the cells for 24 h (D1) resulted in readily detectable fluorescent YFP-ATXN1(Q82) signal (Fig. 1C). Following quantification by flow cytometry, cells at D1 were 84.1% positive for YFP fluorescence signal (Figs. 1D) and 95% after 48 h (D2) of induction. The induced cells produced high levels of YFP-ATXN1(Q82) after 48hrs (D2). An identical molecular weight band (~130 kDa) was also detectable with an anti-GFP antibody (Fig. 1E), corresponding to the exogenous YFP-tagged polyQ-expanded protein, and not the endogenous ATXN1.

We also investigated whether Tet-On YFP-ATXN1(Q82) MSCs retain their mesenchymal phenotype. As indicated by flow cytometry, uninduced/D0 cells were negative for Cluster of Differentiation (CD) markers of the hematopoietic lineage (CD34 and CD45). In contrast, they were >95% double positive for CD markers of the mesenchymal lineage (CD29, CD73, CD90 and CD105) (Supplementary Fig. 1). This

indicates that SB-mediated genetic modification did not affect the mesenchymal properties of the stable lines.

3.2. The pathogenic ATXN1 forms specific annular IIBs in MSCs

Next, we studied the morphology of YFP-ATXN1(Q82) IIBs at different time-points post induction. Cells accumulated small inclusions at D2 that increased in size and partially fused by day 5 (D5). At this point, inclusions consisted of distinct subdomains and seemed to expand around a brighter central core. At day 10 (D10), IIBs adopted an annular structure and dramatically increased in size, occupying most of the nucleus (Fig. 2A). Annular IIBs were also formed in neural progenitor cells (NPCs) derived from healthy iPSCs (Supplementary Fig. 2A). However, only a few of them contained fluorescent inclusions at D10 post induction, suggesting that iPSC-derived NPCs, by contrast to MSCs, may efficiently remove small inclusions or suppress long-term production of the pathogenic ATXN1. Therefore, further experiments were performed using genetically-modified MSCs.

In order to investigate whether polyQ-expansions in ATXN1 are responsible for the annular structure of IIBs, we also generated an inducible control MSC line, producing the wild-type protein YFP-ATXN1(Q30). YFP-ATXN1(Q30) formed spherical IIBs which also increased in size upon prolonged induction with Dox (Supplementary Fig. 2B). However, in contrast to mutant ATXN1, these IIBs did not adopt an annular shape at D10. Therefore, ATXN1 with an expanded polyQ tract specifically forms annular IIBs in MSCs.

To analyze the solubility of ATXN1 proteins, equal amounts of Tet-On YFP-ATXN1(Q30) as well as YFP-ATXN1(Q82) MSC extracts, were analyzed by SDS-PAGE. While, soluble YFP-ATXN1(Q30) and YFP-
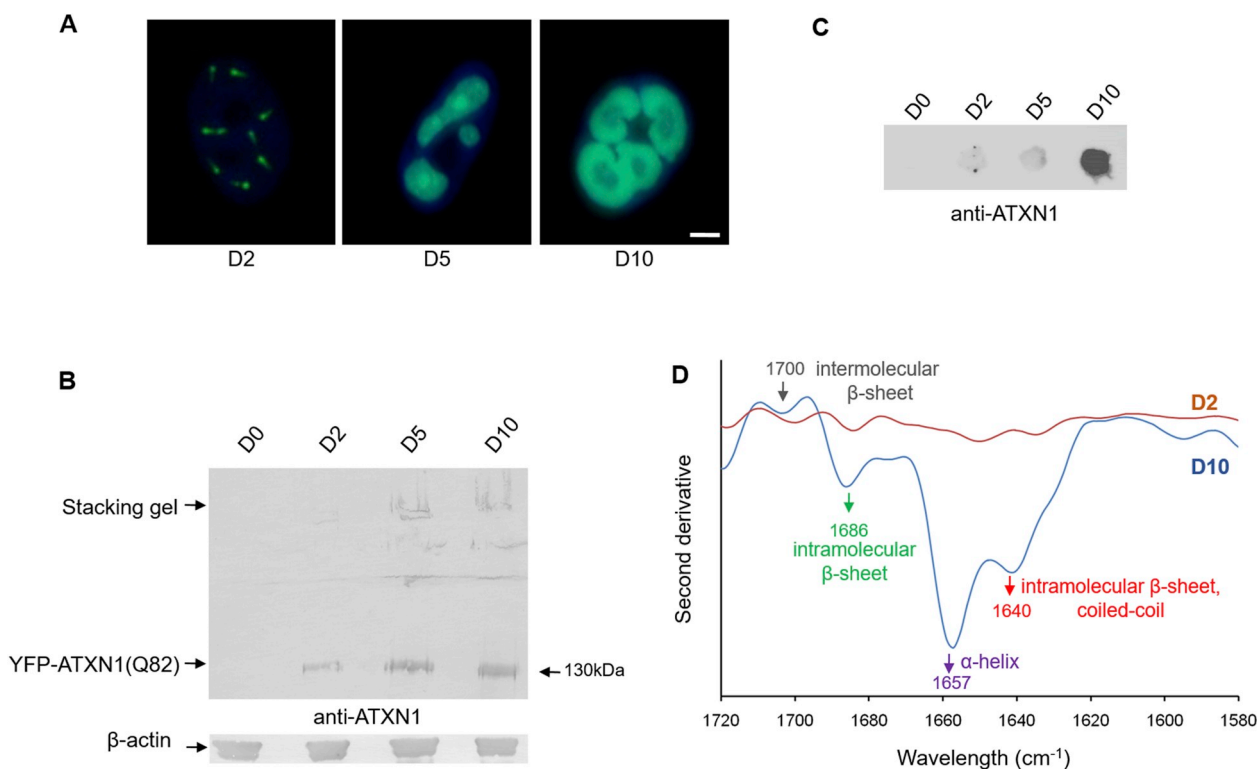
Fig. 2. MSCs expressing YFP-*ATXN1(Q82)* accumulate insoluble IIBs. **(A)** Fluorescence microscopy of Tet-On YFP-ATXN1(Q82) MSCs at D2-D10. Nuclei are stained with DAPI (blue color) (scale bar = 10 μm). **(B–C)** Immunoblots for ATXN1 in **B.** SDS-PAGE and **C.** Filter retardation assays using extracts of uninduced or induced cells. β-actin was used as loading control. **(D)** Second derivative of the FTIR absorption spectrum of Tet-On YFP-ATXN1(Q82) MSCs at D2 or D10. Spectra were corrected after subtraction of the Venus MSCs spectrum. The D10 spectrum shows a peak at 1657 cm^{-1} indicative of α-helix conformation and three peaks at 1640, 1686 and 1700 cm^{-1}, corresponding to coiled-coils, intra- and inter-molecular β-sheets in ATXN1(Q82). (For interpretation of the references to color in this figure legend, the reader is referred to the Web version of this article.)

ATXN1(Q82) were detected at the expected molecular weight at D2, D5 and D10 (Supplementary Fig. 2C and 2B, lower band), a fraction of YFP-ATXN1(Q82) appeared in a higher molecular weight region of the gel in extracts from D5 and D10 cells. These protein species failed to enter the resolving gel or accumulated at the bottom of the well of the loading gel (Fig. 2B). Finally, we examined whether YFP-ATXN1(Q82) IIBs are detectable in a filter retardation assay. This method allows quantification of large, insoluble SDS-stable protein inclusions [25]. Pathogenic ATXN1(Q82) readily formed SDS-stable inclusions at D10 (Fig. 2C), whereas no such inclusions were immunodetected in MSCs inducibly producing YFP-ATXN1(Q30) (Supplementary Fig. 2D). Taken together, these data indicate that mutant ATXN1 forms insoluble IIBs in MSCs with a potential pathogenic conformation after prolonged induction.

3.3. ATXN1(Q82) IIBs are enriched in coiled-coils and β-sheets

We then sought to investigate whether pathogenic ATXN1 adopts a β-sheet conformation in IIBs. To do so, we determined the nominal FTIR absorption spectrum of Tet-On YFP-ATXN1(Q82) MSCs at D10 and observed typical peaks for the main biological macromolecules (Supplementary Fig. 3). Proteins were detected by two different absorption peaks corresponding to amide I and II signals (1400-1800 cm^{-1}) that are related to the C═O stretching vibration of the peptide bond [38]. Similar absorption spectra were also obtained from Tet-On YFP-ATXN1(Q82) MSCs at D0 or D2 (Supplementary Fig. 3).

The measurement from D0 cells was taken as background and subtracted from the absorption spectrum of Tet-On YFP-ATXN1(Q82) MSCs at D2 or D10. The second derivative of the corrected spectra showed no distinct peaks in the range of amide I at D2 in YFP-*ATXN1(Q82)* expressing MSCs. This indicates that these cells contain proteins with a similar conformation to D0 MSCs. In contrast, Tet-On

YFP-ATXN1(Q82) MSCs at D10 exhibited strong peaks at 1657, 1640 and 1686 cm^{-1} (Supplementary Fig. 4). The distinct high-intensity peak at 1657 cm^{-1} may be attributed to α-helical protein structures [38] of YFP-ATXN1(Q82). However, the peak at 1640 cm^{-1} combined with a low-intensity peak at 1685 cm^{-1} suggests an enrichment for coiled-coils [39] and β-sheets [40,41] in the aggregated polyQ-expanded protein.

To exclude the possibility that these peaks result from the fluorescent protein tag, a Venus-tagged MSC line, stably producing a fluorescent variant of YFP [42], was generated as a control. The absorption spectrum of Venus MSCs (Supplementary Fig. 3) was subtracted from the relevant spectra of Tet-On YFP-ATXN1(Q82) MSCs at D2 or D10 and their second derivatives are illustrated in Fig. 2D. The spectrum of D10 Tet-On YFP-ATXN1(Q82) MSCs showed strong peaks at 1657, 1640 and 1686 cm^{-1} along with an additional low peak at 1700 cm^{-1}. No such peaks were observed in D2 cells. These results suggest that the detected peaks can be attributed merely to polyQ-expanded ATXN1. Furthermore, the peaks at 1640 and 1686 cm^{-1} indicate that aggregated YFP-ATXN1(Q82) is enriched in coiled-coils and intra-molecular β-sheets, while the 1700 cm^{-1} peak suggests that the pathogenic protein also forms inter-molecular β-sheets in IIBs [40,43]. This finding suggests that the insolubility of YFP-ATXN1(Q82) IIBs (Fig. 2C) is due to the enrichment of the number of coiled-coils, intra- and inter-molecular β-sheets in the pathogenic protein.

3.4. Intranuclear accumulation of ATXN1(Q82) IIBs affects the mechanical properties of MSCs

Next, we determined the biophysical properties of YFP-*ATXN1(Q82)* expressing MSCs using AFM. This method provides structural, mechanical and functional information of non-stained cells
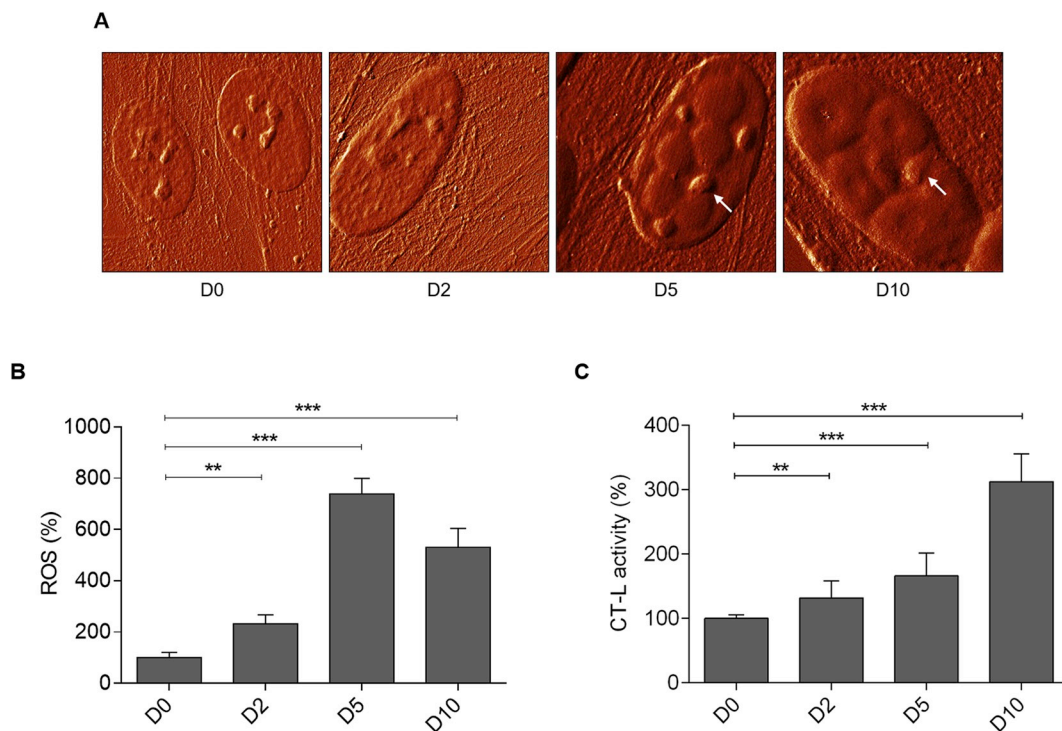
Fig. 3. Cellular effects of YFP-ATXN1(Q82) IIBs. **(A)** Detailed view of the cell nucleus. Cells at D0-D10 were fixed and visualized by AFM in hybrid mode (Quantitative Imaging). White arrows indicate natural nuclear content (nucleoli). The white scale bar in the right image is equal to 20 μm. Z-scaling of all images ranges from 85 to 190 mN/m **(B–C)** Percentages of **(B)** ROS and **(C)** CT-L proteasome activity in uninduced and induced Tet-On YFP-ATXN1(Q82) MSCs at D2, D5 and D10. ROS levels and CT-L activity of control cells (D0) were arbitrarily set to 100%. Error bars denote ±SEM (** p-value < 0.01, *** p-value < 0.001).

or molecules at high resolution under physiological conditions [44,45]. The occupied nuclear area was similar in D0 and D2 MSCs indicating that polyQ inclusions were not detectable by AFM at these time-points. In contrast, a significant increase of the nuclear content was observed in D5 and D10 MSCs (Supplementary Fig. 5A). In the contact mode images, the nuclear content appeared above the threshold (blue masked area). Quantification of the masked area revealed an approximately 12-fold increase in occupied nuclear surface area of D10 MSCs compared to D0 cells (Supplementary Fig. 5B). These data illustrate that the growth of YFP-ATXN1(Q82) IIBs can be efficiently quantified by AFM. Hybrid mode AFM images provided a detailed visualization of the nuclear content. Processing of force-distance curves by the surface distribution of the slope of indentation curve, allowed us to distinguish between natural nuclear structures (e.g. nucleoli - marked with the white arrow) and polyQ inclusions (Fig. 3A). Overlay of AFM and fluorescence images showed that the marked structures were non-fluorescent (Supplementary Fig. 6) excluding the possibility that they represent smaller polyQ protein inclusions. These images indicate that annular IIBs compress the nucleoli (Fig. 3A), suggesting that the accumulation of YFP-ATXN1(Q82) may interfere with their physiological function.

Mechanical properties of Tet-On YFP-ATXN1(Q82) MSCs were studied using the force-volume/nanoindentation method [30,46]. The Young's modulus (stiffness) of D0 and D10 MSCs was compared. There was no significant difference when Young's modulus of whole cells was compared (10.2 ± 2.8 kPa and 23 ± 15 kPa, for D0 and D10 cells, respectively), possibly due to the small occupied area of protein inclusions. However, a significant difference was observed when only the area containing IIBs was compared with the stiffness of an uninduced cell (10.2 ± 2.8 kPa and 36 ± 19 kPa for D0 and D10 cells, respectively, p-value < 0.01) (Supplementary Figs. 7A–B). Similarly, the topography of these cells was compared. Using the set point height technique, YFP-ATXN1(Q82) IIBs were efficiently detected only in D10 MSCs (Supplementary Fig. 7C).

3.5. Accumulation of large ATXN1(Q82) IIBs is an irreversible process

We then investigated whether polyQ inclusions are cytotoxic. Activated caspase 3/7 was measured in Tet-On YFP-ATXN1(Q82) MSCs in the presence or absence of Dox. Induced cells showed similar levels of caspase activity compared to uninduced cells at all time-points (Supplementary Fig. 8). Deposition of YFP-ATXN1(Q82) IIBs does not induce apoptosis in these cells. Nevertheless, after prolonged (10 days) induction, Tet-On YFP-ATXN1(Q82) MSCs acquired an enlarged and flattened phenotype typical of senescent cells. By D20, the majority of cells lost their proliferative capacity and transited towards a growth-arrested state. IIBs were readily visible by optical microscopy (Supplementary Fig. 9A, white arrows); however, they did not significantly increase in size compared to D10. Cells did not die; they rather maintained this state for up to 30 days post induction. These findings suggest that the intranuclear accumulation of mutant ATXN1 does not result in the activation of apoptosis but rather affects the normal cell cycle of MSCs.

Then, we tested whether aggregation of YFP-ATXN1(Q82) induces oxidative stress in MSCs. As shown in Fig. 3B, production of the pathogenic polyQ protein for 2 days resulted in a significant increase in the levels of ROS. This effect was significantly enhanced in both D5 and D10 cells (~7- or 5-fold higher ROS levels, respectively compared to D0 MSCs). Since oxidative stress induces alterations in the protein degradation machinery, chymotrypsin-like (CT-L) activity of the proteasome was measured. CT-L activity was enhanced in D2 cells and further elevated at later time-points. D10 cells showed approximately 3-fold higher proteasome activity compared to D0 MSCs (Fig. 3C). To check if the aggregation was reversible, we asked whether removal of Dox from induced cells would result in the clearance of polyQ inclusions. Tet-On YFP-ATXN1Q82MSCs were induced for 10 days; they were then cultured for 5 additional days in medium without Dox. Cells containing large YFP-ATXN1(Q82) IIBs failed to dissolve them (Supplementary Fig. 9B), indicating that aggregated polyQ proteins are resistant to
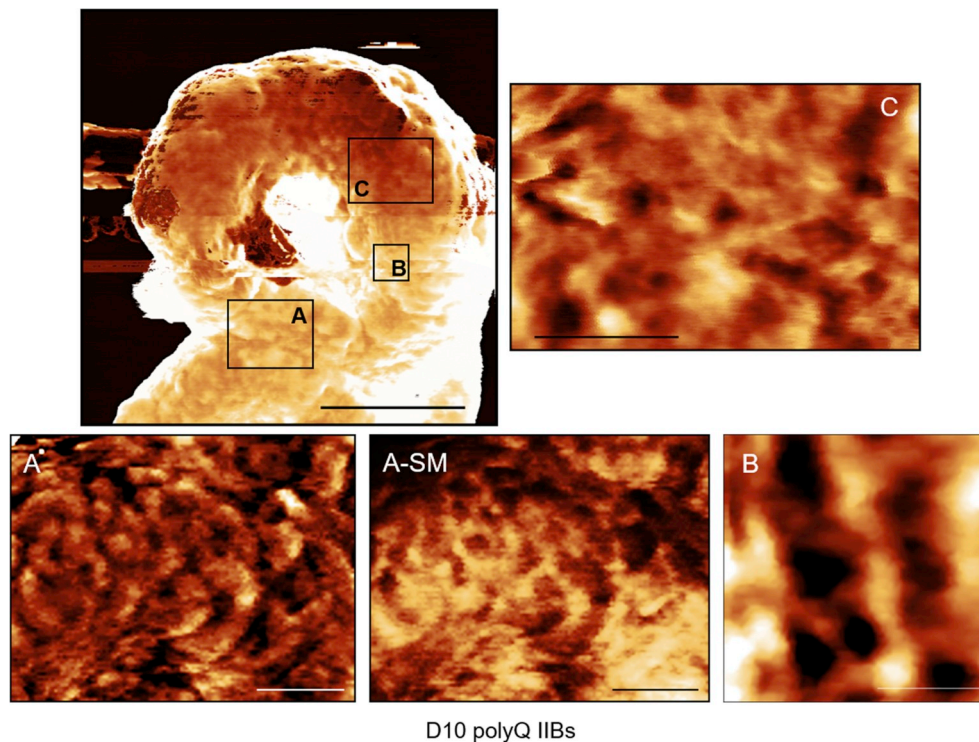
Fig. 4. Detailed view of polyQ ATXN1 protein inclusions visualized *in-situ*. IIBs from Tet-On YFP-ATXN1(Q82) at D10 were immobilized on a plastic surface after lysis of cells in 0.1% SDS PBS. Measurements were performed in isotonic PBS by AFM hybrid mode imaging. Closer view of different parts of an IIB is shown below the main image in **A–C**. **A-SM** shows the distribution of stiffness over the area of image **A**. Inserted scale bars and Z-scale ranges are as follows: main image 3 μm/100 nm, (**A**) 1 μm/15 nm, (**A-SM**) 1 μm/3–130 MPa, (**B**) 300 nm/30 nm and (**C**) 750 nm/30 nm.

D10 polyQ IIBs

degradation. This observation supports our finding that Tet-On YFP-ATXN1(Q82) MSCs at D10 contain insoluble IIBs (Fig. 2C–D).

3.6. Insoluble ATXN1(Q82) IIBs recruit proteins associated with neurodegenerative processes

Based on our finding that polyQ inclusions are insoluble in SDS (Fig. 2C), we sought to isolate and characterize them. Intact annular inclusions of YFP-ATXN1(Q82) at D10 were observed by fluorescence microscopy and AFM (Supplementary Fig. 10A). A detailed view of the inclusion surface using AFM hybrid mode indicated the presence of a lamellar structure (Fig. 4A and C). A higher magnification also showed the presence of pores between the layers of the inclusion (Fig. 4B). The average height of an inclusion was 14.8 ± 5.2 nm. Stiffness measurement on a 6 μm^2 area of the polyQ inclusion showed the distribution of Young's modulus with an average value of 33.6 MPa (Fig. 4A-SM).

Annular polyQ inclusions were then purified from extracts by particle sorting. Efficient isolation was validated post-sorting by flow cytometry (Supplementary Fig. 10B). Proteins recruited into polyQ inclusions were identified by mass spectrometry (MS). In total, 303 different proteins were detected (Supplementary Table 1A) including proteasome and ribosome subunits, ubiquitin-related enzymes and heat-shock proteins. We identified proteins with nuclear localization such as histones, heterogeneous nuclear ribonucleoproteins and nucleophosmin, indicating the nuclear origin of the isolated inclusions. GO enrichment analysis showed that the majority of the identified proteins fall into two distinct clusters, neutrophil degranulation/exocytosis and translation (Supplementary Table 1B) and are functionally similar with protein components of polyQ-expanded Httex1 inclusions (Supplementary Table 1C) [4,10,47,48]. Notably, pathway analysis using the PANTHER database showed that the fraction of proteins recruited into insoluble polyQ IIBs is significantly enriched for the terms Parkinson's and Huntington's disease (Table 1), supporting their relevance for neurodegenerative disease modeling.

3.7. Partially soluble and insoluble ATXN1(Q82) IIBs generate different transcriptional responses

ATXN1 is an RNA-binding protein participating in transcriptional regulation [49,50]. Therefore, we investigated transcriptional changes induced by its overexpression in MSCs. Transcriptome profiles of D0-D10 cells were generated and compared to those of Venus MSCs. Genes with a similar expression profile in both overexpression models (Supplementary Fig. 11A) were excluded from downstream analysis. This experimental setup identified 3,984 differentially expressed (DE) genes (hereafter, ATXN1-DE) due to YFP-*ATXN1(Q82)* overexpression (Supplementary Table 2). Gene Set Enrichment Analysis (GSEA) of ATXN1-DE genes dysregulated in D2 compared to Venus MSCs (|log$_2$fold change| ≥ 1, p-value < 0.05) indicated that expression of the mutant *ATXN1* significantly affected genes encoding proteins with nuclear localization (Supplementary Table 3).

Principal component analysis (PCA) indicated that D2, D5 and D10 cells had a distinct expression profile compared to D0. D2 cells were also distinct from D5 and D10 MSCs, which grouped closely and shared a more common expression profile (Fig. 5A). ATXN1-DE clusters included 611, 682 and 687 genes for D2, D5 and D10, respectively and 1040 unique genes in total. The majority of genes were down-regulated (Fig. 5B). A total of 296 genes (28.5%) were found to be dysregulated at all time-points compared to D0 cells. Pathway term enrichment analysis using the KEGG database showed that these genes were enriched in components of the ribosome or the PI3K-Akt signaling pathway (Fig. 5C and Supplementary Table 4A).

The identity of 148 genes (14.2% of 1,040 genes) specifically dysregulated in D2 cells was investigated. GO Biological Process (BP) indicated several genes involved in positive regulation of neuron apoptotic process (Supplementary Table 4B). Interestingly, analysis of genes dysregulated specifically in D5 and D10 cells (181 genes, 17.4% of the 1,040 genes) revealed a set involved in the opposite process, negative regulation of neuron apoptotic process (Supplementary Table 4C). This indicates that soluble YFP-ATXN1(Q82) produced in MSCs at the early time-point (D2) has a different effect in cells than the partially insoluble protein which forms IIBs at later time-points (D5 and D10). We also

Table 1
Pathway enrichment analysis of proteins detected in insoluble polyQ IIBs.

Enrichment term	Overlap	p-value	Genes/Proteins
Cytoskeletal regulation by Rho GTPase (P00016)	12/70	< 0.0001	TUBB2B; TUBB6; ACTC1; TUBB3; TUBB; CFL1; ARPC4-TTLL3; MYH9; PFN1; TUBB4B; MYH10; ACTG1
Integrin signaling pathway (P00034)	15/156	< 0.0001	ITGB1; ARF1; ACTN1; COL12A1; FN1; ACTN4; ACTG1; COL1A1; COL3A1; COLA2; COL6A1; FLNA; FLNB; TLN1; VCL
Parkinson's disease (P00049)	11/81	< 0.0001	HSPA9; YWHAE; PSMA5; HSPA8; UCHL; HSPA5; YWHAQ; YWHAB; YWHAZ; YWHAG; PSMA7
Huntington's disease (P00029)	10/124	< 0.0001	ARF4; TUBB6; TUBB2B; ARF1; ACTC1; TUBB3; TUBB; TUBB4B; GAPDH; ACTG1
Glycolysis (P00024)	6/17	< 0.0001	TPI1; PKM; PGK1; ENO1; ALDOA; GAPDH

Top five statistically significant enriched pathway terms and overlap of identified genes/proteins with the components of the pathway. The analysis was performed using the PANTHER database.

investigated the identity of 115 genes (11.1% of the 1040 genes) exclusively dysregulated in D10 cells containing insoluble IIBs. GO Cellular Component (CC) analysis revealed enrichment terms for PML body and other subnuclear structures (Supplementary Table 4D) that are associated with response to oxidative stress [51]. This is in agreement with our observation that production of mutant ATXN1 induces oxidative stress in MSCs (Fig. 3B) and the related cell response pathways. These data illustrate the complexity of the dynamic processes that occur in cells expressing pathogenic *ATXN1* in consecutive time-points.

Enrichment analysis using the KEGG database on the significantly dysregulated ATXN1-DE genes at D2 indicated that up-regulated genes participate in ECM-receptor interaction or focal adhesion, while down-regulated genes were involved in the ribosome, DNA replication, cell cycle and oxidative phosphorylation. Importantly, a significant number of down-regulated genes participate in pathways related to neurodegenerative diseases, validating our polyQ protein aggregation model

(Table 2A).

Regarding cellular pathways that were affected by the accumulation of insoluble IIBs in MSCs, we compared D10 and D2 MSCs (S11B Fig). Up-regulated genes were enriched in functions related to protein digestion and absorption and AGE-RAGE, PI3K-Akt, p53 signaling pathways. In contrast, down-regulated genes were involved in DNA replication and cell cycle (Table 2B), consistent with our observation that MSCs containing insoluble IIBs enter a growth-arrest phase (Supplementary Fig. 9A).

3.8. Tet-On YFP-ATXN1(Q82) MSCs share transcriptional similarities with human SCA1 cerebellum

Does our inducible YFP-ATXN1(Q82) MSC system share transcriptional changes with a pathogenic SCA1 human cerebellum? To answer this question, we performed RNA-seq in post-mortem cerebellar tissue
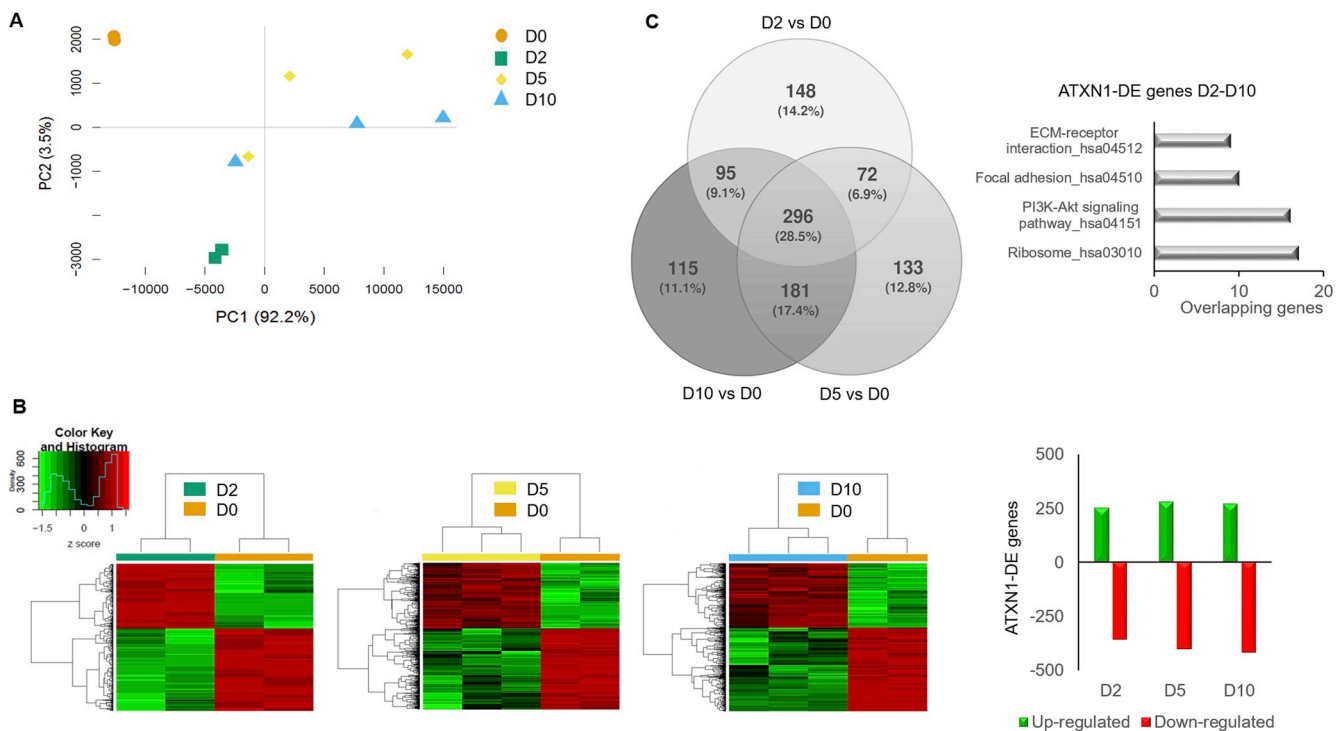
Fig. 5. Transcriptional changes in Tet-On YFP-AXN1(Q82) MSCs containing IIBs. **(A)** Principal Component Analysis (PCA) of the expression vectors of the 3,984 genes specifically dysregulated in Tet-On YFP-AXN1(Q82) MSCs in four time-points according to their PC1 and 2 coordinates. Percentages (%) indicate the proportion of variance of analyzed data per axis. **(B)** Hierarchical clustering analysis and heatmap of ATXN1-DE genes between cells at D2, D5 or D10 vs D0 ($|\log_2$fold change$| \geq 1$ and p-value < 0.05). Each row represents one gene and each column one sample. Figure also shows the absolute numbers of up- or down-regulated ATXN1-DE genes in each time point. **(C)** Venn diagram showing the overlap of ATXN1-DE genes per comparison (described in **B**). KEGG pathway enrichment analysis of ATXN1-DE genes at all time points (D2-D10) is also shown.

Table 2

Pathway enrichment analysis of up- or down-regulated genes in Tet-On YFP-ATXN1(Q82) MSCs containing polyQ IIBs.

A. D2 versus D0

Up-regulated			Down-regulated		
Enrichment term	Overlap	p-value	Enrichment term	Overlap	p-value
ECM-receptor interaction_hsa04512	12/82	>0.0001	Ribosome_hsa03010	30/137	>0.0001
Focal adhesion_hsa04510	16/202	>0.0001	DNA replication_hsa03030	6/36	>0.0001
PI3K-Akt signaling pathway_hsa04151	18/341	>0.0001	Alzheimer's disease_hsa05010	10/168	0.0010
Proteoglycans in cancer_hsa05205	13/203	>0.0001	Cell cycle_hsa04110	8/124	0.0018
Rap1 signaling pathway_hsa04015	13/211	>0.0001	Oxidative phosphorylation_hsa00190	8/133	0.0028
Regulation of actin cytoskeleton_hsa04810	12/214	>0.0001	Huntington's disease_hsa05016	9/193	0.0084

B. D10 versus D2

Up-regulated			Down-regulated		
Enrichment term	Overlap	p-value	Enrichment term	Overlap	p-value
Protein digestion and absorption_hsa04974	7/90	0.0001	DNA replication_hsa03030	4/36	0.0003
AGE-RAGE signaling pathway in diabetic complications_hsa04933	6/101	0.0008	Cell cycle_hsa04110	7/124	0.0002
PI3K-Akt signaling pathway_hsa04151	9/341	0.0114	p53 signaling pathway_hsa04115	5/69	0.0004
p53 signaling pathway_hsa04115	4/69	0.0064	Axon guidance_hsa04360	6/127	0.0012
Lysosome_hsa04142	5/123	0.0104	Wnt signaling pathway_hsa04310	6/142	0.0020
Transcriptional misregulation in cancer_hsa05202	6/180	0.0131	MAPK signaling pathway_hsa04010	7/255	0.0095

Statistically significant enriched pathway terms for up- or down-regulated genes in the relevant comparisons (**A.** D2 versus D0 and **B.** D10 versus D2) and the overlap with the components of the pathway. The analysis was performed using the KEGG database.

both from a late stage SCA1 patient diagnosed with dementia and spinal cerebellar atrophy with polyglutamine inclusions, and from an age/sex-matched healthy individual. This comparative approach identified 3,923 dysregulated genes in the SCA1 patient ($|\log_2 \text{fold change}| \geq 1$), hereafter named as SCA1-DE genes (Supplementary Table 5). GSEA showed that this dataset was enriched for genes encoding nuclear proteins (Supplementary Table 6), similar to our findings in MSCs overexpressing YFP-*ATXN1(Q82)* (Supplementary Table 3).

PolyQ protein inclusions are mainly detected in the cerebellum of SCA1 patients [1]. We therefore compared the patient data with the D10 ATXN1-DE genes in cells containing insoluble IIBs. The down-regulated SCA1-DE and ATXN1-DE genes participate in several common pathways, including cell cycle, oxidative phosphorylation or pathways involved in RNA metabolism (e.g. ribosome, spliceosome and RNA transport) (Table 3A). Similarly, common pathways were identified between the up-regulated genes of the two sets. The up-regulated SCA1-DE genes participate mainly in focal adhesion, as also observed for up-regulated ATXN1-DE genes (Table 3B).

We also found that 27% (185/687) of the dysregulated D10 ATXN1-DE genes were shared with the SCA1-DE gene set. As indicated by KEGG enrichment analysis, the commonly dysregulated genes included genes involved in the ribosomal function (Supplementary Tables 7A–B). Collectively, these results indicate that the transcriptional changes at end-stage human SCA1 cerebellum resemble the cellular response observed in MSCs containing insoluble IIBs of the mutant ATXN1 at D10.

3.9. ATXN1(Q82) IIBs perturb the ribosomal protein interaction network

The protein inclusions in neurodegenerative diseases produce pathogenic effects due to a trapping effect [52]. According to this hypothesis, protein inclusions act as molecular "black-holes", trapping proteins along with their downstream interactors. We sought to model this scenario by investigating the PPI network of the ATXN1-DE proteins.

To gain insights into the perturbation of PPIs caused by insoluble IIBs, we used the dataset of dysregulated D10 ATXN1-DE genes and compared it to a cerebellum-specific human PPI network, using HIPPIE v2.0 [37]. This database collects interactions between human proteins scored according to the reliability of the associated experimental evidence. High-confidence interactions (HIPPIE score ≥ 0.63) were considered between the products of the D10 versus D0 ATXN1-DE genes

that were expressed in the cerebellum [37], the most affected tissue in SCA1 disorder [53]. The resulting network was formed by 516 gene products.

Importantly, the subnetwork containing the largest connected component (LCC) of the constructed PPI network had a statistically significant LCC size (p-value = 8.03×10^{-4}, 328 proteins, Supplementary Table 8) when compared to a randomly sampled control network (Fig. 6A). This strategy identified a highly interconnected PPI module that was perturbed by the dysregulation of gene expression and induced by the accumulation of insoluble polyQ IIBs in cells. Most of the proteins in the LCC are down-regulated and their functional enrichment analysis points to the perturbation of key proteins required for proper ribosome assembly and translation (Fig. 6B–C). The most densely connected region of the LCC is formed, almost entirely, by ribosomal subunits whose protein levels are significantly reduced in D10 MSCs containing insoluble IIBs (Table 4 and Supplementary Table 9). Also, a significant fraction of the proteins identified in polyQ inclusions (Supplementary Table 1) is also part of the LCC (n = 33, p-value $< 2 \times 10^{-16}$), further supporting the role of IIBs in the disruption of nucleolus-related functions. Intriguingly, this network also contains 109 human SCA1-DE components (p-value $< 2 \times 10^{-16}$, Fig. 6C and Supplementary Table 8), indicating their potential relevance for SCA1 pathogenesis. Thus, these data support the hypothesis that the pathogenic effect of the mutant ATXN1 in our cell model is associated with the trapping of key protein synthesis factors and their interactors by the polyQ IIBs.

4. Discussion

4.1. Inducible, Sleeping Beauty transposon-based expression of ATXN1(Q82) in human MSCs

Cellular protein aggregation models are invaluable to elucidate the pathogenic effects of polyQ IIBs in neurodegenerative diseases, including SCA1. These models are also important for screening assays and for drug development [13]. SCA1 patient-derived iPSCs [54], differentiated into cerebellar neurons [55] provide an opportunity for studying disease progression in the exact match of the affected cell type. Nevertheless, the developmental reset occurring upon iPSC derivation erases aging-associated signatures [56], which may interfere with the aggregation process occurring in adult neurons. In fact, in the context of

Table 3

Pathway enrichment analysis of down- and up-regulated genes in human SCA1 cerebellum and D10 Tet-On YFP-ATXN1(Q82) MSCs.

A. Down-regulated

SCA1 patient versus control			D10 versus D0 cells		
Enrichment term	Overlap	p-value	Enrichment term	Overlap	p-value
Protein processing in endoplasmic reticulum_hsa04141	66/169	>0.0001	Ribosome_hsa03010	32/137	>0.0001
Spliceosome_hsa03040	52/134	>0.0001	Huntington's disease_hsa05016	12/193	0.0008
RNA degradation_hsa03018	31/77	>0.0001	DNA replication_hsa03030	5/36	0.0009
Cell cycle_hsa04110	41/124	>0.0001	Cell cycle_hsa04110	9/124	0.0012
RNA transport_hsa03013	52/172	>0.0001	Alzheimer's disease_hsa05010	10/168	0.0029
Proteasome_hsa03050	20/44	>0.0001	Parkinson's disease_hsa05012	9/142	0.0030
Protein export_hsa03060	13/23	>0.0001	Non-alcoholic fatty liver disease (NAFLD)_hsa04932	9/151	0.0045
Ubiquitin mediated proteolysis_hsa04120	42/137	>0.0001	Oxidative phosphorylation_hsa00190	8/133	0.0069
FoxO signaling pathway_hsa04068	40/133	>0.0001	Nucleotide excision repair_hsa03420	4/47	0.0165
DNA replication_hsa03030	15/36	0.0002	Spliceosome_hsa03040	7/134	0.0227
Non-homologous end-joining_hsa03450	8/13	0.0003	Pyrimidine metabolism_hsa00240	6/105	0.0229
mRNA surveillance pathway_hsa03015	28/91	0.0003	Ubiquitin mediated proteolysis_hsa04120	7/137	0.0252
Nucleotide excision repair_hsa03420	16/47	0.0018	RNA transport_hsa03013	8/172	0.0285
Oxidative phosphorylation_hsa00190	34/133	0.0029	Fatty acid biosynthesis_hsa00061	2/13	0.029
Ribosome_hsa03010	34/137	0.0049	Base excision repair_hsa03410	3/33	0.0311

B. Up-regulated

SCA1 patient versus control			D10 versus D0 cells		
Enrichment term	Overlap	p-value	Enrichment term	Overlap	p-value
Focal adhesion_hsa04510	20/202	>0.0001	Focal adhesion_hsa04510	17/202	>0.0001
Chronic myeloid leukemia_hsa05220	11/73	0.0001	ECM-receptor interaction_hsa04512	11/82	>0.0001
Hippo signaling pathway_hsa04390	16/153	0.0001	PI3K-Akt signaling pathway_hsa04151	17/341	>0.0001
Cell adhesion molecules (CAMs)_hsa04514	15/142	0.0002	Proteoglycans in cancer_hsa05205	11/203	>0.0001
Notch signaling pathway_hsa04330	8/48	0.0003	Protein digestion and absorption_hsa04974	8/90	>0.0001
AGE-RAGE signaling pathway in diabetic complications_hsa04933	11/101	0.0011	Regulation of actin cytoskeleton_hsa04810	11/214	0.0002
Proteoglycans in cancer_hsa05205	17/203	0.0012	Pathways in cancer_hsa05200	15/397	0.0003
Regulation of actin cytoskeleton_hsa04810	17/214	0.0021	Rap1 signaling pathway_hsa04015	10/211	0.0006
Long-term potentiation_hsa04720	8/66	0.0025	Phagosome_hsa04145	7/154	0.0049
ECM-receptor interaction_hsa04512	9/82	0.0028	Leukocyte transendothelial migration_hsa04670	6/118	0.0053
Inositol phosphate metabolism_hsa00562	8/71	0.0040	Glioma_hsa05214	4/65	0.0114
ErbB signaling pathway_hsa04012	9/87	0.0042	AGE-RAGE signaling pathway in diabetic complications_hsa04933	5/101	0.0118

The table shows statistically significant enriched pathway terms for **A.** down- or **B.** up-regulated genes in the relevant comparisons and the overlap with the components of the pathway. The analysis was performed using the KEGG database.

Huntington's disease, protein aggregation could be detected in neurons directly derived from fibroblasts but not in neurons differentiated from iPSCs [57]. In line with these findings, we observed that iPSC-derived NPCs efficiently removed small inclusions and failed to support long-term production of the pathogenic ATXN1.

As an alternative approach, our inducible polyQ-expanded ATXN1-based model generates reproducibly large nuclear inclusions in human MSCs. This model overexpresses the full-length *ATXN1(Q82)*, harboring all domains that affect protein dimerization and aggregation [58,59] in an inducible manner, using the Tet-On SB transposon system. The SB system is suitable for the modification of human stem cells with high reproducibility [60–62]. In combination with the hyperactive transposase SB100X [15], our Gateway-compatible system [63] can be used for rapid and highly efficient generation of expression vectors. The inducible expression system is not leaky and provides a tight control. It is also suitable for a stable, forced expression of pathogenic transgenes and a reproducible formation of the nuclear IIBs in cultured primary human cells.

Even though MSCs are adult stem cells of mesodermal origin [64] with a limited neurogenic differentiation potential [65], they have several advantages compared to immortalized laboratory lines previously utilized to study polyQ protein aggregation [9,66]. These cells can be modified using the SB system and cultured in cost-effective conditions [17,18]. More importantly, MSCs are resistant to the proteotoxic insults of ATXN1(Q82), which allowed a detailed investigation of the gradual accumulation of the toxic protein. Also, MSCs are subjected to replicative senescence, a phenomenon that resembles aging

[67] and promotes polyQ protein aggregation. Thus, MSCs proved to be a proper choice in our studies aiming at characterizing the IIB formation of the pathogenic ATXN1.

4.2. ATXN1(Q82) gradually forms insoluble IIBs in MSCs

Prolonged induction of MSCs resulted in the formation of partially insoluble IIBs. Using AFM, we established a set of methods to efficiently measure nuclear coverage, determine topology of IIBs and quantify cell stiffness in non-stained cells at different stages of their formation. In our cell model, purified annular IIBs exhibit a significantly lower stiffness compared to polyQ aggregates prepared *in vitro* [68,69], suggesting that they contain a decreased amount of amyloid fibrils. However, the annular structure might be a common feature of insoluble IIBs. Such inclusions have been observed in cell-free systems and transgenic mouse models of polyQ diseases [70,71], indicating that they are polyQ length-dependent and are specifically induced by the pathogenic protein.

Accumulation of the pathogenic ATXN1 was accompanied by discrete changes in the expression profiles of nuclear proteins. This observation is consistent with the topology of IIBs. Importantly, our inducible ATXN1(Q82) MSCs are suitable to model both the early and late stage effects of protein aggregation (D2 vs D10). For example, components of the focal adhesion complex were up-regulated at the early stage [e.g. D2 ATXN1(Q82) MSCs], genes of the PI3K-Akt pathway were constantly up in D2-D10, while members of the p53 signaling pathway specifically featured in the late stage.
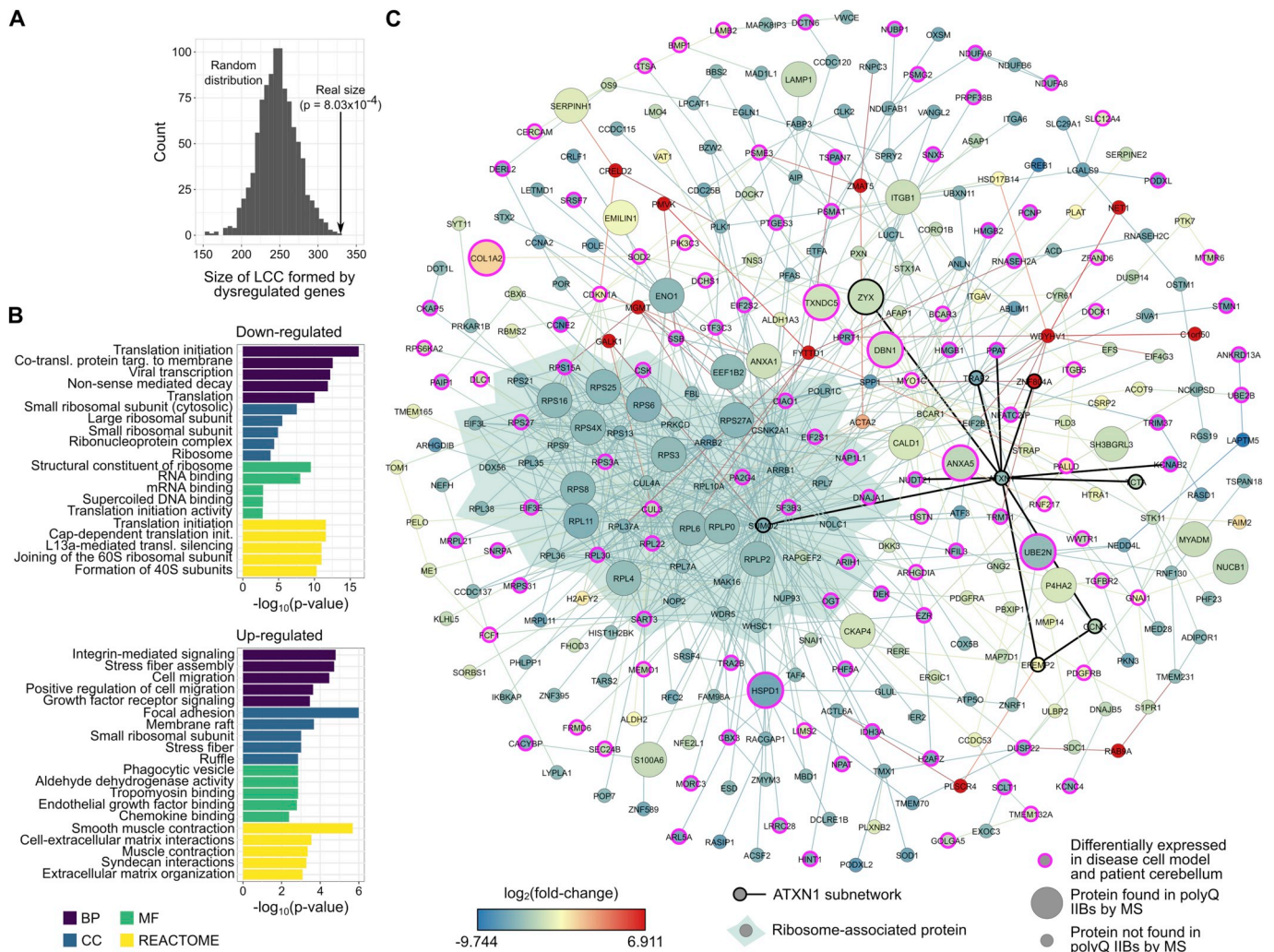
Fig. 6. ATXN1 IIBs dysregulate ribosome assembly and translation-associated protein interactions. **(A)** ATXN1-DE genes significantly dysregulated between D10 and D0 cells form a highly interconnected PPI network module (largest connected component or LCC) whose size (black arrow) is significantly greater than expected by chance. **(B)** The down-regulated members of this LCC play important roles in ribosome assembly and translation. By contrast, the up-regulated members of the LCC are involved in cellular organization functions and compartments. **(C)** The LCC of the constructed cerebellum-specific PPI network has a densely connected region formed almost entirely by ribosomal subunits and contains a significant number of proteins detected by MS in the insoluble IIBs at D10 (n = 33, p-value < 0.001). This depiction also highlights the interaction partners of ATXN1 in the LCC and human SCA1-DE genes (n = 109, p-value < 0.001, magenta color). Expression levels of each gene in the disease cell model are also shown. (For interpretation of the references to color in this figure legend, the reader is referred to the Web version of this article.)

The downregulation of genes participating in oxidative phosphorylation may cause defects in the respiratory chain of both the MSCs and the cerebellar cells of the SCA1 patient. These defects may be responsible for the cellular oxidative stress while the activation of proteasome can be considered as a secondary line of defense against it. Our findings are consistent with the stimulation of ROS production by aggregating polyQ-expanded proteins [5,72] and connect to early hypotheses implicating oxidative stress in the pathology of neurodegenerative diseases [73].

The accumulation of IIBs also interferes with the nucleolus, suggesting that MSCs undergo nucleolar stress [74] and eventually enter a growth-arrest phase. This hypothesis is consistent with the down-regulation of genes involved in DNA replication and cell cycle, generally observed here and in models of polyQ diseases [75]. In fact, proteins oligomers were shown to dysregulate the cell cycle through the PI3K-Akt pathway [76] which promotes necrotic cell death [77].

4.3. PolyQ-induced stress perturbs the protein synthesis machinery

PolyQ tracts are normally present in a significant percentage of human proteins. Experimental evidence suggests that these domains mediate PPIs during the assembly of protein complexes [78]. Pathogenic polyQ proteins are enriched in coiled-coils [22,79] and spontaneously self-assemble into insoluble β-sheet rich inclusions [59,80] which are cytotoxic when they are transported into the nucleus [81]. The enrichment of aggregated ATXN1(Q82) in coiled-coils and β-sheets, suggests that insoluble IIBs might act as scaffolds for the sequestration of various protein molecules, perturbing protein interaction networks. The recruitment of ribosomal proteins and nucleophosmin, a nucleolar-stress marker which is critical for ribosome biogenesis [82] in insoluble IIBs indicates that these proteins are not able to perform their normal functions. In parallel, the down-regulation of ribosomal gene expression depletes the available ribosomal proteins in cells containing insoluble IIBs. Our results indicate a perturbed cerebellum-specific PPI network, which contains a densely connected subnetwork formed by components

involved in RNA metabolism and protein synthesis.

Even though polyQ diseases may not share the same pathology at early stages, perturbation of the ribosomal complex might be a common feature at a later stage. PolyQ oligomers recruit ribosomal proteins [4,47] and promote the cytosolic mislocalization of fibrillarin (Fbl), a nucleolar protein involved in rRNA processing [47]. The combination of these events results in the retention of ribosomal proteins in the nucleus and prevents proper ribosome biogenesis. Furthermore, nucleolar stress induced by pathogenic misfolded proteins results in the extensive oxidation of ribosomal RNA, the reduction of ribosomes and the decrease in protein synthesis [reviewed in Ref. [74]]. Eventually, insoluble polyQ inclusions may cause similar mechanical and molecular defects in cells containing them.

We propose a series of events induced by the pathogenic ATXN1, including (a) down-regulation of ribosomal genes; (b) gradual induction of oxidative and nucleolar stress by expanding IIBs; and (c) sequestration of ribosomal proteins into insoluble IIBs. Altogether, these events cause defects in RNA metabolism, ribosome assembly and protein synthesis leading to cell necrosis (Fig. 7). Notably, our findings correlate with the effects of the glutamine-rich PQN-41C protein in *C. elegans*. PQN-41C forms non-toxic cytoplasmic aggregates and controls non-apoptotic developmental cell death [83], supporting the hypothesis that similar mechanisms might be activated by polyQ-expanded proteins in vertebrates. Furthermore, the disturbed PPI network presented here, contains a significant number of genes that are dysregulated in human SCA1 cerebellum. Experimental data indicate that disrupted homeostasis of ribosomes triggers dendritic degeneration and disconnection of neuronal circuitries [84]. In the long-term, perturbation of the protein synthesis machinery may cause dysfunction of cerebellar neurons driving them towards a necrotic state in SCA1.

5. Conclusions

Our study establishes a nuclear aggregation model of pathogenic ATXN1, the causative mutation of the SCA1 disease. Using an inducible SB-based expression system in MSCs, we generated primary human cells gradually accumulating insoluble IIBs. We show that IIBs generate cellular oxidative stress and characterized their structure and morphology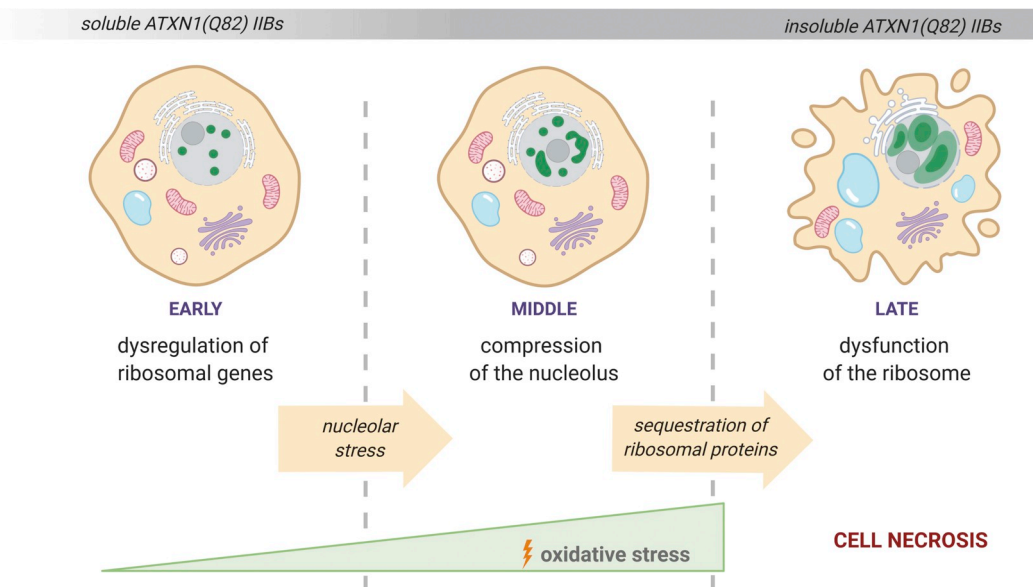. Furthermore, we identified the transcriptional changes induced by the presence of polyQ-expanded ATXN1, which are partially observed in end-stage SCA1 cerebellum, as well. The transcriptional changes in senescent cells containing insoluble IIBs indicate a cerebellum-specific perturbed protein interaction network involved in protein synthesis. Our model can be utilized for detailed investigations of the biochemical pathways affecting polyQ protein aggregation and the development of protective approaches against it.

Authors' contributions

Conceived and designed the experiments: SL GAL JP TR NC SPos ZIz PS MAA SP. Performed the experiments: SL JP TR BT KM GK ML. Analyzed the data: SL GAL JP TR KM MT JO GK MS FP. Contributed material: AZ AP ZIv ZIz. Wrote the paper: SP GAL JP GK. Edited the manuscript: SL TR MT JO NC AP ZIv SPos ZIz PS MAA. Designed the study: SP. All authors read and approved the final manuscript.

Funding

Fig. 7. Cellular events caused by the gradual formation of insoluble ATXN1(Q82) IIBs. Production of ATXN1(Q82) dysregulates ribosomal genes and causes oxidative and nucleolar stress at early stages of protein aggregation. Expanding IIBs (shown with green color) compress the nucleolus and sequester ribosomal proteins. Eventually, insoluble ATXN1(Q82) IIBs disrupt the biogenesis of ribosomes and cause cell necrosis. (For interpretation of the references to color in this figure legend, the reader is referred to the Web version of this article.)

Table 4

Protein levels of LCC ribosome components in cells containing insoluble polyQ IIBs.

Protein Name	Accession #	log$_2$fold change D10 versus D0	p-value	adj. p-value
Ataxin-1	P54253	9.05	>0.001	>0.001
Eukaryotic translation initiation factor 2 subunit 1	P05198	−0.51	>0.001	0.001
Eukaryotic translation initiation factor 3 subunit E	P60228	−0.53	>0.001	0.001
Eukaryotic translation initiation factor 3 subunit L	Q9Y262	−0.60	>0.001	0.001
rRNA 2′-O-methyltransferase fibrillarin	P22087	−0.17	0.036	0.065
60S ribosomal protein L4	P36578	−0.50	>0.001	0.001
60S ribosomal protein L6	Q02878	−0.56	>0.001	0.001
60S ribosomal protein L7	P18124	−0.63	>0.001	0.001
60S ribosomal protein L7a	P62424	−0.32	0.014	0.030
60S ribosomal protein L10a	P62906	−0.60	>0.001	0.001
60S ribosomal protein L11	P62913	−0.70	>0.001	0.001
60S ribosomal protein L22	P35268	−0.63	>0.001	0.001
60S ribosomal protein L30	P62888	−0.66	>0.001	0.002
60S ribosomal protein L35	P42766	−0.65	>0.001	0.001
60S ribosomal protein L36	Q9Y3U8	−0.54	>0.001	0.002
60S ribosomal protein L37a	P61513	−0.50	>0.001	0.002
60S ribosomal protein L38	P63173	−0.25	0.009	0.021
60S acidic ribosomal protein P0	P05388	−0.59	>0.001	>0.001
60S acidic ribosomal protein P2	P05387	−0.62	>0.001	0.001
40S ribosomal protein S3	P23396	−0.73	>0.001	0.001
40S ribosomal protein S3a	P61247	−0.64	>0.001	0.001
40S ribosomal protein S4, X isoform	P62701	−0.61	>0.001	0.001
40S ribosomal protein S6	P62753	−0.67	>0.001	0.000
40S ribosomal protein S8	P62241	−0.63	>0.001	>0.001
40S ribosomal protein S9	P46781	−0.61	>0.001	0.001
40S ribosomal protein S13	P62277	−0.62	>0.001	0.001
40S ribosomal protein S15a	P62244	−0.62	>0.001	0.001
40S ribosomal protein S16	P62249	−0.45	0.002	0.006
40S ribosomal protein S21	P63220	−0.88	>0.001	0.001
40S ribosomal protein S25	P62851	−0.64	>0.001	>0.001
40S ribosomal protein S27	P42677	−1.08	>0.001	>0.001
Ubiquitin-40S ribosomal protein S27a	P62979	0.52	>0.001	0.001

The table shows the log$_2$fold change in the protein levels of LCC components which are related to protein synthesis.

Declaration of competing interest

The authors declare no commercial or financial conflict of interest.

Appendix A. Supplementary data

Supplementary data to this article can be found online at https://doi.org/10.1016/j.redox.2020.101458.

References

[1] H.T. Orr, H.Y. Zoghbi, SCA1 molecular genetics: a history of a 13 year collaboration against glutamines, Hum. Mol. Genet. 10 (20) (2001) 2307–2311.

[2] P.J. Skinner, B.T. Koshy, C.J. Cummings, I.A. Klement, K. Helin, A. Servadio, et al., Ataxin-1 with an expanded glutamine tract alters nuclear matrix-associated structures, Nature 389 (6654) (1997) 971–974.

[3] T. Takahashi, S. Kikuchi, S. Katada, Y. Nagai, M. Nishizawa, O. Onodera, Soluble polyglutamine oligomers formed prior to inclusion body formation are cytotoxic, Hum. Mol. Genet. 17 (3) (2008) 345–356.

[4] Y.M. Ramdzan, M.M. Trubetskov, A.R. Ormsby, E.A. Newcombe, X. Sui, M.J. Tobin, et al., Huntingtin inclusions trigger cellular quiescence, deactivate apoptosis, and lead to delayed necrosis, Cell Rep. 19 (5) (2017) 919–927.

[5] A. Bertoni, P. Giuliano, M. Galgani, D. Rotoli, L. Ulianich, A. Adornetto, et al., Early and late events induced by polyQ-expanded proteins: identification of a common pathogenic property of polYQ-expanded proteins, J. Biol. Chem. 286 (6) (2011) 4727–4741.

[6] K.A. Burke, J. Legleiter, Atomic force microscopy assays for evaluating polyglutamine aggregation in solution and on surfaces, Methods Mol. Biol. 1017 (2013) 21–40.

[7] P.R. Dahlgren, M.A. Karymov, J. Bankston, T. Holden, P. Thumfort, V.M. Ingram, et al., Atomic force microscopy analysis of the Huntington protein nanofibril formation, Nanomed. Nanotechnol. Biol. Med. 1 (1) (2005) 52–57.

[8] W.C. Duim, B. Chen, J. Frydman, W.E. Moerner, Sub-diffraction imaging of huntingtin protein aggregates by fluorescence blink-microscopy and atomic force microscopy, ChemPhysChem : a European journal of chemical physics and physical chemistry 12 (13) (2011) 2387–2390.

[9] F.J.B. Bauerlein, I. Saha, A. Mishra, M. Kalemanov, A. Martinez-Sanchez, R. Klein, et al., In situ architecture and cellular interactions of PolyQ inclusions, Cell 171 (1) (2017) 179–187 e10.

[10] A. Gruber, D. Hornburg, M. Antonin, N. Krahmer, J. Collado, M. Schaffer, et al., Molecular and structural architecture of polyQ aggregates in yeast, Proc. Natl. Acad. Sci. U. S. A. 115 (15) (2018) E3446–E3453.

[11] P. Koch, P. Breuer, M. Peitz, J. Jungverdorben, J. Kesavan, D. Poppe, et al., Excitation-induced ataxin-3 aggregation in neurons from patients with Machado-Joseph disease, Nature 480 (7378) (2011) 543–546.

[12] S.K. Hansen, T.C. Stummann, H. Borland, L.F. Hasholt, Z. Tumer, J.E. Nielsen, et al., Induced pluripotent stem cell - derived neurons for the study of spinocerebellar ataxia type 3, Stem Cell Res. 17 (2) (2016) 306–317.

[13] E.K. Siska, G. Koliakos, S. Petrakis, Stem cell models of polyglutamine diseases and their use in cell-based therapies, Front. Neurosci. 9 (2015) 247.

[14] F. Huda, Y. Fan, M. Suzuki, A. Konno, Y. Matsuzaki, N. Takahashi, et al., Fusion of human fetal mesenchymal stem cells with "degenerating" cerebellar neurons in spinocerebellar ataxia type 1 model mice, PloS One 11 (11) (2016) e0164202.

[15] L. Mates, M.K. Chuah, E. Belay, B. Jerchow, N. Manoj, A. Acosta-Sanchez, et al., Molecular evolution of a novel hyperactive Sleeping Beauty transposase enables robust stable gene transfer in vertebrates, Nat. Genet. 41 (6) (2009) 753–761.

[16] M. Hudecek, Z. Izsvak, S. Johnen, M. Renner, G. Thumann, Z. Ivics, Going non-viral: the Sleeping Beauty transposon system breaks on through to the clinical side, Crit. Rev. Biochem. Mol. Biol. 52 (4) (2017) 355–380.

[17] M. Kapetanou, N. Chondrogianni, S. Petrakis, G. Koliakos, E.S. Gonos, Proteasome activation enhances stemness and lifespan of human mesenchymal stem cells, Free Radic. Biol. Med. 103 (2016) 226–235.

[18] E.K. Siska, I. Weisman, J. Romano, Z. Ivics, Z. Izsvak, U. Barkai, et al., Generation of an immortalized mesenchymal stem cell line producing a secreted biosensor protein for glucose monitoring, PloS One 12 (9) (2017) e0185498.

[19] V. Trachana, S. Petrakis, Z. Fotiadis, E.K. Siska, V. Balis, E.S. Gonos, et al., Human mesenchymal stem cells with enhanced telomerase activity acquire resistance against oxidative stress-induced genomic damage, Cytotherapy 19 (7) (2017) 808–820.

[20] J. Saarikangas, Y. Barral, Protein aggregates are associated with replicative aging without compromising protein quality control, eLife 4 (2015).

[21] S. Petrakis, T. Rasko, L. Mates, Z. Ivics, Z. Izsvak, K. Kouzi-Koliakou, et al., Gateway-compatible transposon vector to genetically modify human embryonic kidney and adipose-derived stromal cells, Biotechnol. J. 7 (7) (2012) 891–897.

[22] S. Petrakis, T. Rasko, J. Russ, R.P. Friedrich, M. Stroedicke, S.P. Riechers, et al., Identification of human proteins that modify misfolding and proteotoxicity of pathogenic ataxin-1, PLoS Genet. 8 (8) (2012) e1002897.

[23] C. Lorenz, P. Lesimple, R. Bukowiecki, A. Zink, G. Inak, B. Mlody, et al., Human iPSC-derived neural progenitors are an effective drug discovery model for neurological mtDNA disorders, Cell stem cell 20 (5) (2017) 659–674 e9.

[24] P. Reinhardt, M. Glatza, K. Hemmer, Y. Tsytsyura, C.S. Thiel, S. Hoing, et al., Derivation and expansion using only small molecules of human neural progenitors for neurodegenerative disease modeling, PloS One 8 (3) (2013) e59252.

[25] E.E. Wanker, E. Scherzinger, V. Heiser, A. Sittler, H. Eickhoff, H. Lehrach, Membrane filter assay for detection of amyloid-like polyglutamine-containing protein aggregates, Methods Enzymol. 309 (1999) 375–386.

[26] D. Ami, A. Natalello, S.M. Doglia, Fourier transform infrared microspectroscopy of complex biological systems: from intact cells to whole organisms, Methods Mol. Biol. 895 (2012) 85–100.

[27] N. Chondrogianni, I. Petropoulos, C. Franceschi, B. Friguet, E.S. Gonos, Fibroblast cultures from healthy centenarians have an active proteasome, Exp. Gerontol. 35 (6–7) (2000) 721–728.

[28] J.L. Gilmore, A. Yoshida, H. Takahashi, K. Deguchi, T. Kobori, E. Louvet, et al., Analyses of nuclear proteins and nucleic acid structures using atomic force microscopy, Methods Mol. Biol. 1262 (2015) 119–153.

[29] M. Golan, S. Jelinkova, I. Kratochvilova, P. Skladal, M. Pesl, V. Rotrekl, et al., AFM monitoring the influence of selected cryoprotectants on regeneration of cryopreserved cells mechanical properties, Front. Physiol. 9 (2018) 804.

[30] G. Nardone, J. Oliver-De La Cruz, J. Vrbsky, C. Martini, J. Pribyl, P. Skladal, et al., YAP regulates cell mechanics by controlling focal adhesion assembly, Nat. Commun. 8 (2017) 15321.

[31] D. Necas, P. Klapetek, Gwyddion: an open-source software for SPM data analysis, Cent. Eur. J. Phys. 10 (1) (2012) 181–188.

[32] J.R. Wisniewski, A. Zougman, N. Nagaraj, M. Mann, Universal sample preparation method for proteome analysis, Nat. Methods 6 (5) (2009) 359–362.

[33] J. Cox, M.Y. Hein, C.A. Luber, I. Paron, N. Nagaraj, M. Mann, Accurate proteome-wide label-free quantification by delayed normalization and maximal peptide ratio extraction, termed MaxLFQ. Molecular & cellular proteomics, MCP 13 (9) (2014) 2513–2526.

[34] M. Pertea, D. Kim, G.M. Pertea, J.T. Leek, S.L. Salzberg, Transcript-level expression analysis of RNA-seq experiments with HISAT, StringTie and Ballgown, Nat. Protoc. 11 (9) (2016) 1650–1667.

[35] G. Yu, L.G. Wang, Y. Han, Q.Y. He, clusterProfiler: an R package for comparing biological themes among gene clusters, OMICS A J. Integr. Biol. 16 (5) (2012) 284–287.

[36] M.V. Kuleshov, M.R. Jones, A.D. Rouillard, N.F. Fernandez, Q. Duan, Z. Wang, et al., Enrichr: a comprehensive gene set enrichment analysis web server 2016 update, Nucleic Acids Res. 44 (W1) (2016) W90–W97.

[37] G. Alanis-Lobato, M.A. Andrade-Navarro, M.H. Schaefer, HIPPIE v2.0: enhancing meaningfulness and reliability of protein-protein interaction networks, Nucleic Acids Res. 45 (D1) (2017) D408–D414.

[38] J.L. Arrondo, F.M. Goni, Structure and dynamics of membrane proteins as studied by infrared spectroscopy, Prog. Biophys. Mol. Biol. 72 (4) (1999) 367–405.

[39] T. Heimburg, J. Schuenemann, K. Weber, N. Geisler, Specific recognition of coiled coils by infrared spectroscopy: analysis of the three structural domains of type III intermediate filament proteins, Biochemistry 35 (5) (1996) 1375–1382.

[40] A. Natalello, A.M. Frana, A. Relini, A. Apicella, G. Invernizzi, C. Casari, et al., A major role for side-chain polyglutamine hydrogen bonding in irreversible ataxin-3 aggregation, PLoS One 6 (4) (2011) e18789.

[41] M. Tanaka, I. Morishima, T. Akagi, T. Hashikawa, N. Nukina, Intra- and inter-molecular beta-pleated sheet formation in glutamine-repeat inserted myoglobin as a model for polyglutamine diseases, J. Biol. Chem. 276 (48) (2001) 45470–45475.

[42] A. Rekas, J.R. Alattia, T. Nagai, A. Miyawaki, M. Ikura, Crystal structure of venus, a yellow fluorescent protein with improved maturation and reduced environmental sensitivity, J. Biol. Chem. 277 (52) (2002) 50573–50578.

[43] G. Zandomeneghi, M.R. Krebs, M.G. McCammon, M. Fandrich, FTIR reveals structural differences between native beta-sheet proteins and amyloid fibrils, Protein Sci. 13 (12) (2004) 3314–3321.

[44] A. Trache, G.A. Meininger, Atomic force microscopy (AFM), Curr Protoc Microbiol (2008) 2C.2.1-2C.2.17.

[45] S. Vahabi, B. Nazemi Salman, A. Javanmard, Atomic force microscopy application in biological research: a review study, Iran. J. Med. Sci. 38 (2) (2013) 76–83.

[46] G. Thomas, N.A. Burnham, T.A. Camesano, Q. Wen, Measuring the mechanical properties of living cells using atomic force microscopy, JoVE 76 (2013).

[47] Y.E. Kim, F. Hosp, F. Frottin, H. Ge, M. Mann, M. Hayer-Hartl, et al., Soluble oligomers of PolyQ-expanded huntingtin target a multiplicity of key cellular factors, Mol. Cell 63 (6) (2016) 951–964.

[48] J. Kim, H.J. Waldvogel, R.L. Faull, M.A. Curtis, L.F. Nicholson, The RAGE receptor and its ligands are highly expressed in astrocytes in a grade-dependant manner in the striatum and subependymal layer in Huntington's disease, J. Neurochem. 134 (5) (2015) 927–942.

[49] X. Tong, H. Gui, F. Jin, B.W. Heck, P. Lin, J. Ma, et al., Ataxin-1 and Brother of ataxin-1 are components of the Notch signalling pathway, EMBO Rep. 12 (5) (2011) 428–435.

[50] S. Yue, H.G. Serra, H.Y. Zoghbi, H.T. Orr, The spinocerebellar ataxia type 1 protein, ataxin-1, has RNA-binding activity that is inversely affected by the length of its polyglutamine tract, Hum. Mol. Genet. 10 (1) (2001) 25–30.

[51] U. Sahin, O. Ferhi, M. Jeanne, S. Benhenda, C. Berthier, F. Jollivet, et al., Oxidative stress-induced assembly of PML nuclear bodies controls sumoylation of partner proteins, J. Cell Biol. 204 (6) (2014) 931–945.

[52] F. Hosp, H. Vossfeldt, M. Heinig, D. Vasiljevic, A. Arumughan, E. Wyler, et al., Quantitative interaction proteomics of neurodegenerative disease proteins, Cell Rep. 11 (5) (2015) 1134–1146.

[53] A.H. Koeppen, The pathogenesis of spinocerebellar ataxia, Cerebellum 4 (1) (2005) 62–73.

[54] R.A.M. Buijsen, S.L. Gardiner, M.J. Bouma, L.M. van der Graaf, M.W. Boogaard, B.A. Pepers, et al., Generation of 3 spinocerebellar ataxia type 1 (SCA1) patient-derived induced pluripotent stem cell lines LUMCi002-A, B, and C and 2 unaffected sibling control induced pluripotent stem cell lines LUMCi003-A and B, Stem Cell Res. 29 (2018) 125–128.

[55] Y. Ishida, H. Kawakami, H. Kitajima, A. Nishiyama, Y. Sasai, H. Inoue, et al., Vulnerability of Purkinje cells generated from spinocerebellar ataxia type 6 patient-derived iPSCs, Cell Rep. 17 (6) (2016) 1482–1490.

[56] J. Mertens, D. Reid, S. Lau, Y. Kim, F.H. Gage, Aging in a dish: iPSC-derived and directly induced neurons for studying Brain aging and age-related neurodegenerative diseases, Annu. Rev. Genet. 52 (2018) 271–293.

[57] M.B. Victor, M. Richner, H.E. Olsen, S.W. Lee, A.M. Monteys, C. Ma, et al., Striatal neurons directly converted from Huntington's disease patient fibroblasts recapitulate age-associated disease phenotypes, Nat. Neurosci. 21 (3) (2018) 341–352.

[58] C. de Chiara, R.P. Menon, F. Dal Piaz, L. Calder, A. Pastore, Polyglutamine is not all: the functional role of the AXH domain in the ataxin-1 protein, J. Mol. Biol. 354 (4) (2005) 883–893.

[59] S. Petrakis, M.H. Schaefer, E.E. Wanker, M.A. Andrade-Navarro, Aggregation of polyQ-extended proteins is promoted by interaction with their natural coiled-coil partners, Bioessays 35 (6) (2013) 503–507.

[60] E. Belay, J. Matrai, A. Acosta-Sanchez, L. Ma, M. Quattrocelli, L. Mates, et al., Novel hyperactive transposons for genetic modification of induced pluripotent and adult stem cells: a nonviral paradigm for coaxed differentiation, Stem Cell. 28 (10) (2010) 1760–1771.

[61] C. Jackel, M.S. Nogueira, N. Ehni, C. Kraus, J. Ranke, M. Dohmann, et al., A vector platform for the rapid and efficient engineering of stable complex transgenes, Sci. Rep. 6 (2016) 34365.

[62] E. Kowarz, D. Loscher, R. Marschalek, Optimized Sleeping Beauty transposons rapidly generate stable transgenic cell lines, Biotechnol. J. 10 (4) (2015) 647–653.

[63] J.L. Hartley, G.F. Temple, M.A. Brasch, DNA cloning using in vitro site-specific recombination, Genome Res. 10 (11) (2000) 1788–1795.

[64] M.A. Vodyanik, J. Yu, X. Zhang, S. Tian, R. Stewart, J.A. Thomson, et al., A mesoderm-derived precursor for mesenchymal stem and endothelial cells, Cell stem cell 7 (6) (2010) 718–729.

[65] A. Scuteri, M. Miloso, D. Foudah, M. Orciani, G. Cavaletti, G. Tredici, Mesenchymal stem cells neuronal differentiation ability: a real perspective for nervous system repair? Curr. Stem Cell Res. Ther. 6 (2) (2011) 82–92.

[66] L. Guo, B.I. Giasson, A. Glavis-Bloom, M.D. Brewer, J. Shorter, A.D. Gitler, et al., A cellular system that degrades misfolded proteins and protects against neurodegeneration, Mol. Cell 55 (1) (2014) 15–30.

[67] W. Wagner, S. Bork, P. Horn, D. Krunic, T. Walenda, A. Diehlmann, et al., Aging and replicative senescence have related effects on human stem and progenitor cells, PloS One 4 (6) (2009) e5846.

[68] F.S. Ruggeri, G. Longo, S. Faggiano, E. Lipiec, A. Pastore, G. Dietler, Infrared nanospectroscopy characterization of oligomeric and fibrillar aggregates during amyloid formation, Nat. Commun. 6 (2015) 7831.

[69] F.S. Ruggeri, S. Vieweg, U. Cendrowska, G. Longo, A. Chiki, H.A. Lashuel, et al., Nanoscale studies link amyloid maturity with polyglutamine diseases onset, Sci. Rep. 6 (2016) 31155.

[70] K. Sathasivam, A. Lane, J. Legleiter, A. Warley, B. Woodman, S. Finkbeiner, et al., Identical oligomeric and fibrillar structures captured from the brains of R6/2 and knock-in mouse models of Huntington's disease, Hum. Mol. Genet. 19 (1) (2010) 65–78.

[71] J.L. Wacker, M.H. Zareie, H. Fong, M. Sarikaya, P.J. Muchowski, Hsp 70 and Hsp 40 attenuate formation of spherical and annular polyglutamine oligomers by partitioning monomer, Nat. Struct. Mol. Biol. 11 (12) (2004) 1215–1222.

[72] S. Hands, M.U. Sajjad, M.J. Newton, A. Wyttenbach, In vitro and in vivo aggregation of a fragment of huntingtin protein directly causes free radical production, J. Biol. Chem. 286 (52) (2011) 44512–44520.

[73] M.F. Beal, Aging, energy, and oxidative stress in neurodegenerative diseases, Ann. Neurol. 38 (3) (1995) 357–366.

[74] M. Hetman, M. Pietrzak, Emerging roles of the neuronal nucleolus, Trends Neurosci.

35 (5) (2012) 305–314.

[75] M. Lu, C. Boschetti, A. Tunnacliffe, Long term aggresome accumulation leads to DNA damage, p53-dependent cell cycle arrest, and steric interference in mitosis, J. Biol. Chem. 290 (46) (2015) 27986–28000.

[76] K. Bhaskar, M. Miller, A. Chludzinski, K. Herrup, M. Zagorski, B.T. Lamb, The PI3K-Akt-mTOR pathway regulates Abeta oligomer induced neuronal cell cycle events, Mol. Neurodegener. 4 (2009) 14.

[77] Y.T. Wu, H.L. Tan, Q. Huang, C.N. Ong, H.M. Shen, Activation of the PI3K-Akt-mTOR signaling pathway promotes necrotic cell death via suppression of autophagy, Autophagy 5 (6) (2009) 824–834.

[78] M.H. Schaefer, E.E. Wanker, M.A. Andrade-Navarro, Evolution and function of CAG/polyglutamine repeats in protein-protein interaction networks, Nucleic Acids Res. 40 (10) (2012) 4273–4287.

[79] I. Pelassa, D. Cora, F. Cesano, F.J. Monje, P.G. Montarolo, F. Fiumara, Association of polyalanine and polyglutamine coiled coils mediates expansion disease-related protein aggregation and dysfunction, Hum. Mol. Genet. 23 (13) (2014) 3402–3420.

[80] A.S. Wagner, A.Z. Politi, A. Ast, K. Bravo-Rodriguez, K. Baum, A. Buntru, et al., Self-assembly of mutant huntingtin exon-1 fragments into large complex fibrillar structures involves nucleated branching, J. Mol. Biol. 430 (12) (2018) 1725–1744.

[81] W. Yang, J.R. Dunlap, R.B. Andrews, R. Wetzel, Aggregated polyglutamine peptides delivered to nuclei are toxic to mammalian cells, Hum. Mol. Genet. 11 (23) (2002) 2905–2917.

[82] K. Itahana, K.P. Bhat, A. Jin, Y. Itahana, D. Hawke, R. Kobayashi, et al., Tumor suppressor ARF degrades B23, a nucleolar protein involved in ribosome biogenesis and cell proliferation, Mol. Cell 12 (5) (2003) 1151–1164.

[83] E.S. Blum, M.C. Abraham, S. Yoshimura, Y. Lu, S. Shaham, Control of nonapoptotic developmental cell death in Caenorhabditis elegans by a polyglutamine-repeat protein, Science 335 (6071) (2012) 970–973.

[84] L.P. Slomnicki, M. Pietrzak, A. Vashishta, J. Jones, N. Lynch, S. Elliot, et al., Requirement of neuronal ribosome synthesis for growth and maintenance of the dendritic tree, J. Biol. Chem. 291 (11) (2016) 5721–5739.